Dear Dr. Neale and Editors,

We are submitting the revised manuscript gmd-2021-346, titled "Embedding a One-column Ocean Model (SIT 1.06) in the Community Atmosphere Model 5.3 (CAM5.3; CAM5–SIT v1.0) to Improve Madden–Julian Oscillation Simulation in Boreal Winter". Our deepest gratitude goes to the editors and anonymous reviewers for their careful work and thoughtful suggestions that have helped improve this revised manuscript substantially. Additionally, all revision tracks of the manuscript are shown on Pages 18-78.

Sincerely,

Yung-Yao Lan, Huang-Hsiung Hsu, Wan-Ling Tseng, and Li-Chiang Jiang

Research Center for Environmental Changes
Academia Sinica
Taipei, Taiwan

Anonymous Referee #1

The reviewer comments are formatted in italics and the authors response to the comments are formatted in bold.

Notation *RC1.P#* represents Reviewers Comment. Paragraph Number

RC1.general comment 1. This manuscript focuses on the development of a global coupled model on forecasting MJOs. The propagation of MJOs along the equator can significantly affect the precipitation in many regions, so the relevant model works have been devoted by many previous studies. I appreciate the authors' efforts for continuously improving the model forecast on this multi-scale weather system. Unfortunately, one thing I am trying to find in this manuscript is their unique contributions to the broad society. According to the title, it seems like the authors feeling confident in the usage of a 1-D SIT model for predicting MJOs. At the end of Introduction, the authors barely mention their motivation is to "examine how air–sea coupling can improve MJO simulation, especially that of the eastward propagation that has been poorly simulated in many climate models". Because many global coupled models use the 3-D ocean models, the connection between the title (1-D SIT model) and motivation (effect of air-sea coupling on MJO propagation) is unclear. Are the authors trying to convince readers the effect of 1-D model enough for the forecast? Or is there anything special inside the SIT model? The importance of air-sea coupling should have been extensively emphasized and agreed by many studies, and I do not think any ongoing research still trying to use a global model without ocean parts. Repeating the work may be meaningless. I believe their motivation needs to be rewritten.

Response:

Thank you for your comment. We did not attempt to argue that the effect of 1-D model enough for the forecast or simulation of the MJO; instead, we demonstrate that a 1-D model with high vertical resolution in the first 10 meters could have significant improvement. At the end, we suggested that using extra fine vertical resolution in the first few tens of meters of 3-D ocean model could further improve the simulation of the MJO. The improvement due to high resolution had been demonstrated using ECHAM5 (Tseng et al. 2014). This study demonstrated the same effect in CAM5 and suggested that the improvement is not model dependence. By

coupling the 1-D SIT model to an AGCM different from Tseng et al. (2014), this study confirms the scientific reproducibility for the improvement of MJO simulation in modeling science.

We further explored the dependence of the improvement on various factors such as coupling depth, frequency and domain that have not been explored in previous studies, and we considered our results valuable insights for the MJO simulations. We have revised the introduction and summary following the discussion above to state more clearly the motivation and contribution of this study.

RC1.general comment 2. On the other hand, because the authors introduce some models unable to simulate the MJO propagation reliably, I believe one of their expected results is to improve the motion of MJOs (also mentioned in the motivation). However, it seems like the authors do not summarize how much improvements can be seen in their results, or which factors can affect the simulation the most. Because there are some interesting experiments inside this manuscript, such as the coupling regions, I do not think it should be rejected at this moment. However, the structure and quality of the manuscript are very poor. It is very close to my standard for rejection (too many things to be fixed). I only list some problems below, not all. I recommend a major revision for this work in this review.

Response:

Thanks for your suggestion. We summarized specifically in the original (and revised) manuscript what are the better settings and important factors for MJO simulations. We did not attempt to quantify the degree of improvement because it is likely model dependent. Nevertheless, the improvement is evident in many presented figures, e.g., the summarized figure (Figure 10 in revised manuscript) shown in the Summary. The findings are as follows.

(1) Better resolving the fine structure of the upper-ocean temperature and therefore the air–sea interaction led to more realistic intraseasonal variability in both SST

and atmospheric circulation.

(2) An adequate thickness of the oceanic mixed layer is required to simulate a delayed response of the upper ocean to atmospheric forcing and lower-frequency fluctuation.

(3) Coupling the tropical eastern Pacific, in addition to the tropical IO and the tropical WP, can enhance the MJO and facilitate the further eastward propagation of the MJO to the dateline.

(4) Coupling the southern tropical ocean, instead of the norther tropical ocean, is essential for simulating a realistic MJO.

(5) Stronger MJO variability can be obtained without considering the diurnal cycle in coupling.

In general, upper-ocean vertical resolution and coupling with the southern tropical would be of relative importance compared to other factors for the eastward propagation of the MJO.

> *RC1.P1 I do not think conducting an experiment for studying the difference between A-CTL and C-30NS is needed. In my point of view, we do not need another paper talking about the importance of coupling the upper ocean in the global models. In other words, please simplify the description in section 4.1. All you need is to show your coupled model sufficient for simulating the MJOs.*

Response:

The purpose of the comparison between A–CTL and C–30NS was not just to demonstrate again that air–sea coupling could improvement MJO simulation. It also served as the basis for the evaluation of sensitivity experiments that tested the key ingredients for the improvement, in addition to showing that significant improvement in MJO simulation can be achieved by simply coupling a numerically efficient 1-D ocean model. For this purpose, the C–30NS experiment served as a

control coupled experiment is essential. We therefore prefer to retain this experiment and relevant discussion, and hope for reviewer's understanding.

RC1.P2 I am super uncomfortable in the description of the ERA-interim results as the "observation". It is impossible to measure the global wind at 850 hPa directly. Besides, the precipitation data looks like a post-processed product constituted by many satellite measurements. It happens to the OISST as well.

Response:

Thank you for the suggestion. We modified the manuscript to mention directly the name of data used for comparison, instead of referring them as observation. Please see Page 11, lines 244, 247 and 260, Page 12, lines 272, 274 and 280 as well as section 3 in the revised manuscript.

RC1.P3 I think you need to reconsider your structure in the main text. There are some unnecessary and redundant materials that can be moved to the appendix or supplemental material. For example, you do not adjust the coefficients in the 1-D TKE closure scheme. Why do you need to describe the full equations? I also don't care about the numbers of depths from lines 207 to 212 (yes, your units are wrong).

Response:

The comments are well taken. We have removed the background information about SIT and the units are corrected. Thank you for the reminder. Please see Page 7, lines 159-161 and Page 8, lines 162-180 in the revised manuscript.

RC1.P4 You do not need section 3, because people like me already forget the details when we are reading sections since 4.2. Please reorganize the structure.

Response:

Thank you for the suggestion. We feel a brief discussion of experiment setups could be useful for completeness and the readers. Content of Section 3 is now moved to Section 2.3. The essence of each experiment was briefly mentioned again in other sections when relevant results were presented. Detailed information of each experiment is also presented in a table and in supplementary material.

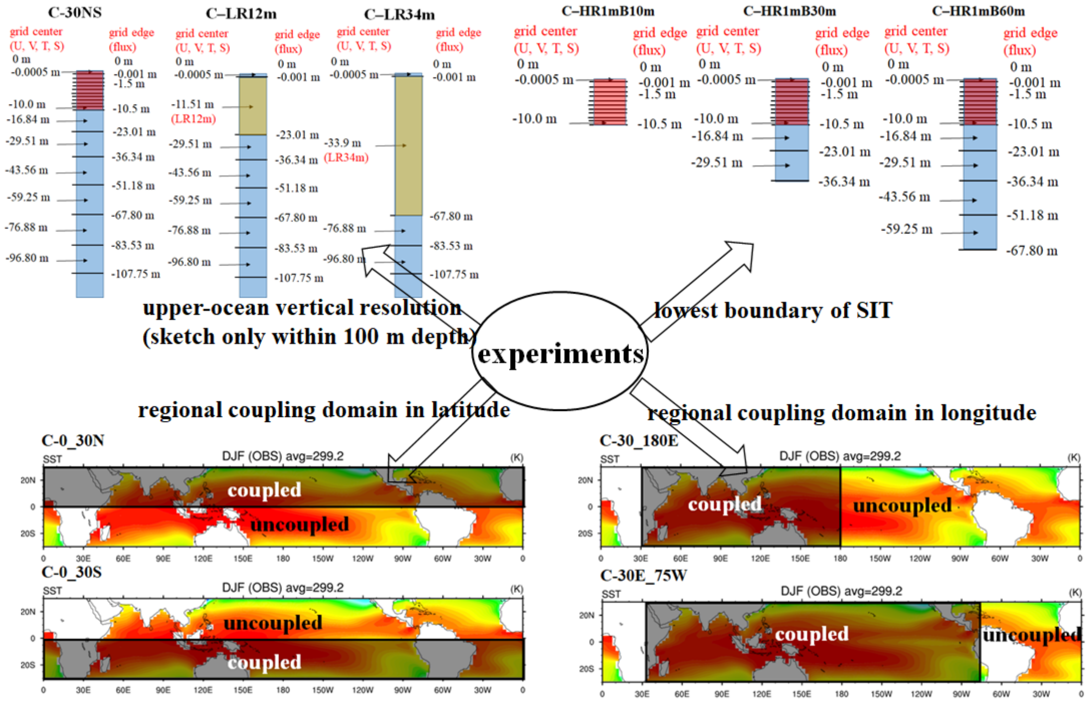

Fig. RC1.1 Schematic diagram of a series of 30-year numerical experiments.

Table 1. List of experiments

Section	Category	Experiments	Description
3.1	Coupled or uncoupled	A–CTL	Standalone CAM5.3 forced by forced by the monthly mean Hadley Centre SST dataset version 1 climatology
		C–30NS (the control coupled experiment)	CAM5.3 coupled with SIT over the tropical domain (30°S–30°N), with 41 layers of finest vertical resolution (up to the seabed) and diurnal cycle; the frequency of CAM5 being exchanged with CPL is 48 times per day
3.2	Upper-ocean vertical resolution	C–LR12m	The first ocean vertical level starts at 11.5 m with 31 layers (beside SST and cool skin layer are 11.5 m, 29.5 m and 43.6 m up to the seabed)
		C–LR34m	The first ocean vertical level starts at 33.9 m with 28 layers (beside SST and cool skin layer are 33.9 m, 76.9 m and 96.8 m up to the seabed)
3.3	Lowest boundary of SIT	C–HR1mB10m	The lowest boundary of SIT has a depth of 10 m (model depth between 0 m and 10 m)
		C–HR1mB30m	The lowest boundary of SIT has a depth of 30 m (model depth between 0 m and 30 m)
		C–HR1mB60m	The lowest boundary of SIT has a depth of 60 m (model depth between 0 m and 60 m)
3.4	Regional coupling domain in latitude	C–0_30N	Coupled in the tropical northern hemisphere (0°N–30°N, 0°E–360°E)
		C–0_30S	Coupled in the tropical southern hemisphere (0°S–30°S, 0°E–360°E)
	Regional coupling domain in longitude	C–30_180E	Coupled in the Indo-Pacific (30°S–30°N, 30°E–180°E)
		C–30E_75W	Coupled over the Indian Ocean and Pacific Ocean (30°S–30°N, 30°E–75°W)
3.5	Absence of the diurnal cycle	C–30NS–nD	Absence of the diurnal cycle in C–30NS; the CAM5.3 daily atmospheric mean of surface wind, temperature, total precipitation, net surface heat flux, u-stress and v-stress over water trigger the SIT and daily mean SST feedback to atmosphere; the frequency of CAM5 is exchanged with CPL 48 times per day

Experiment abbreviations: "A" means standalone AGCM simulation. "C" means the

CAM5.3 coupled to the SIT model.

RC1.P5 I do not think that section 4.2 is discussing the vertical resolution… It is more like the thickness of the first layer. A lot of information is missing here. For example, what is your surface mixed layer depth? If the surface mixed layer depth is less than 30 m or 10 m, what do you do for C-LR34m C-LR12m? Are you trying to test the effect of a slab model in your global coupled model?

Response:

At the first sight, it may seem as reviewer suggested "more like the thickness of the first layer". Although we did not conduct different vertical resolutions within the first 10.5 meters, a comparison between three experiments did suggest that the extra fine resolution in the first 10 meters contribute markedly to the improvement. With a 41-layer vertical discretization in SIT model in the control experiment, 12 layers are located above 10.5 m and 6 layers are located between 10.5 m and 107.8 m. High vertical resolution is needed to catch detailed temporal variation of upper ocean temperature. To test the effect of vertical resolution, we conducted C–LR12m and C–LR34m without vertical discretization in the first layer (Figure RC1.2) to explore the impacts of fine vertical resolution on MJO simulation. This comparison showed that the simulated MJO became more realistic with increasing the upper-ocean vertical resolution. This result has an important implication for the further development of fully coupled GCM that often has the first oceanic layer as thick as 10 meters (e.g., POP2).

The SIT is not a simple slab model that usually has just one layer. As shown in Figure RC1.2, the model is as thick as 107.8 meters and with several layers between surface and model bottom. C–LR12m and C–LR34m have a first layer with grid center at 12m and 34m, respectively, but have the same vertical discretization as in the control experiment (C–30NS). We apologize for the confusion. Figure RC1.2 is

now included in supplementary material. Readers can better understand the experiment setups.

SIT vertical grid mixing processes are based on eddy and molecular diffusivity for heat and momentum. The numerical treatments of C–LR12m (31 vertical layers) and C–LR34m (28 vertical layers) would still be computed from 0 m to seabed if the mixed layer depth was less than 30 m or 10 m.

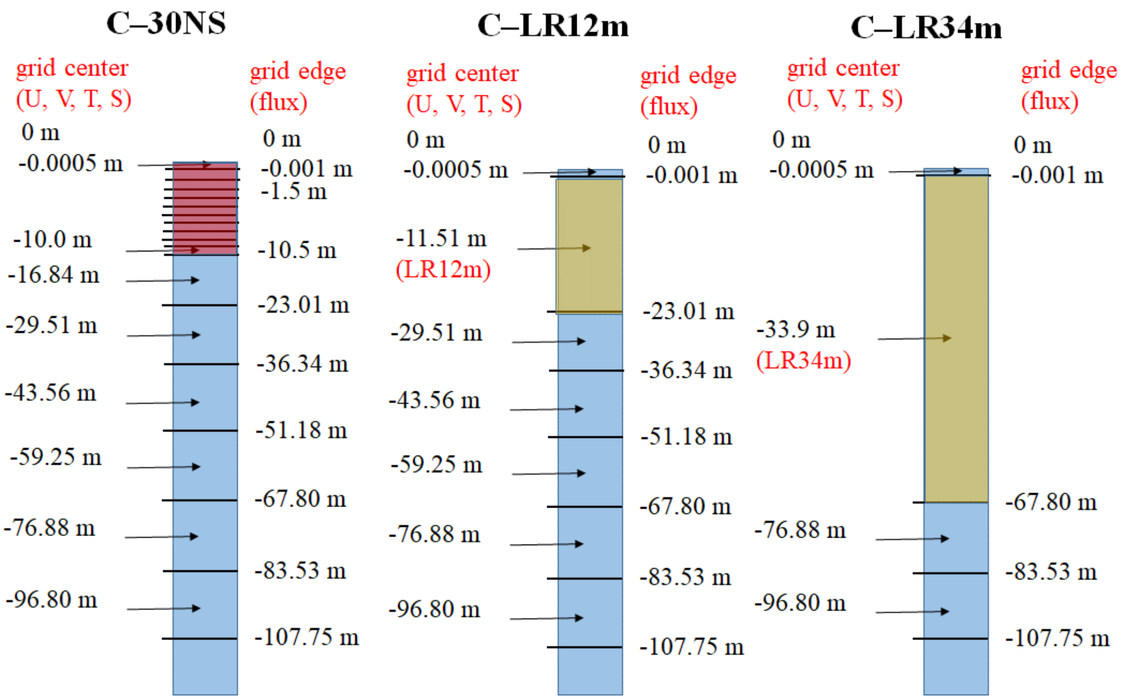

Fig. RC1.2 Diagram showing the vertical grid within 107.8 m in C–30NS, C–LR12m and C–LR34m.

RC1.P6 What do you mean "ocean bottom" at line 476? Is it seafloor?

Response:

Thank you for the question. "Ocean bottom" is misleading. It should be the bottom of the SIT as shown in Fig. RC1.3. Their ocean model bottoms are 10, 30, and 60 m, respectively, unless the seabed is shallower than the above depth. For example, if the seafloor of ocean grid is deeper than 67.8 m, this ocean grid of C–HR1mB60m would be

computed from 0 m to 59.3 m depth. IF the seafloor is 52 m depth in one of C–HR1mB60m ocean grid, this grid would only be computed from 0 m to 43.6 m depth. We have change “ocean bottom” to “ocean model bottom” in the manuscript. Please see Page 9, lines 211-213 and Page 19, line 464 in the revised manuscript.

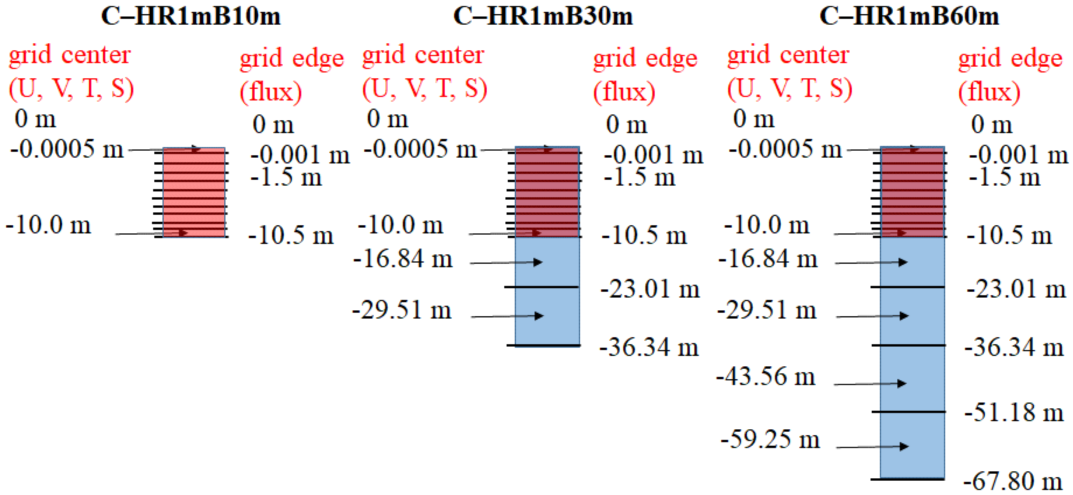

Fig. RC1.3 Diagram showing the totally vertical grids in C–HR1mB10m, C–HR1mB30m and C–HR1mB60m.

RC1.P7 Rewrite section 4.6. I cannot understand which fluxes you are using.

Response:

Heat fluxes here were sensible and latent fluxes that were calculated based on simulated winds, moisture, and temperature. We have modified the text accordingly in revised manuscript. Thank you for the reminder. Please see Page 3, line 50 and Page 22, lines 539-542 in the revised manuscript.

RC1.P8 I cannot understand why the runs are 30 yr? What are the initial conditions of atmosphere and ocean? Is the forcing the same as the values in the real world from 1990-2020?

Response:

A 30-year period is commonly used to define a current climate by the WMO and IPCC (2013) and has been a common length adopted in climate simulations to produce stable statistics. It is natural for us to adopt the same simulation strategy.

All simulations were driven by the same emission and annual cycle of SST for 30 years. The strategy is to evaluate the ability of model under the same conditions without considering interannual variation. This approach has been widely adopted in many studies (Delworth et al., 2006; Haertel et al., 2020; Subramanian et al., 2011; Tseng et al., 2014; Wang et al., 2005). Based on the atmosphere component of the Community Earth System Model version 1.2.2 (CESM1.2.2) framework development, all experiments of CAM5–SIT were conducted under the F_2000_CAM5 component set that provides the near-equilibrium climate responses. The sea surface temperature (SST, HadSST1) used to force the model was the climatological monthly means SST averaged over 1982-2001. The monthly SST was linearly interpolated to daily SST fluctuation that forced the model. The SST in air–sea coupling region was recalculated by SIT during the simulation, while the prescribed annual cycle of SST was used in the areas outside the coupling region.

Atmospheric initial conditions and other external forcing such as CO_2, ozone, and aerosol representing the climate around year 2000 were taken from the default setting of F_2000_CAM5 component set that has been commonly used in present-day simulation using CAM5 (e.g., He et al., 2017). Initital conditions were not needed for the SST that was prescribed as lower boundary condition in the experiments. This information is now included in the revised manuscript.

References:

Delworth, T. L., et al.: GFDL's CM2 global coupled climate models. Part 1: Formulation and simulation characteristics. J. Climate, 19, 643–674, https://doi.org/10.1175/JCLI3629.1, 2006.

Haertel, P.: Prospects for Erratic and Intensifying Madden-Julian Oscillations. Climate, 8, 24, https://doi.org/10.3390/cli8020024, 2020.

He, S., Yang, S. and Li, Z.: Influence of Latent Heating over the Asian and Western Pacific Monsoon Region on Sahel Summer Rainfall, Sci Rep 7, 7680, https://doi.org/10.1038/s41598-017-07971-6, 2017.

IPCC: Annex III: Glossary [Planton, S. (ed.)]. In: Climate Change 2013: The Physical Science Basis. Contribution of Working Group I to the Fifth Assessment Report of the Intergovernmental Panel on Climate Change [Stocker, T.F., D. Qin, G.-K. Plattner, M. Tignor, S.K. Allen, J. Boschung, A. Nauels, Y. Xia, V. Bex and P.M. Midgley (eds.)]. Cambridge University Press, Cambridge, United Kingdom and New York, NY, USA. 2013.

Subramanian, A. C., Jochum, M., Miller, A. J., Murtugudde, R., Neale, R. B., and Waliser, D. E.: The Madden–Julian oscillation in CCSM4, J. Climate, 24, 6261–6282, https://doi.org/10.1175/JCLI-D-11-00031.1, 2011.

Tseng, W.-L., Tsuang, B.-J., Keenlyside, N. S., Hsu, H.-H. and Tu, C.-Y.: Resolving the upper-ocean warm layer improves the simulation of the Madden-Julian oscillation, Clim. Dynam., 44, 1487–1503, https://doi.org/10.1007/s00382-014-2315-1, 2014.

Wang, S. Saha, Pan, H. L., Nadiga, S. and White, G.: Simulation of ENSO in the new NCEP Coupled Forecast System Model (CFS03). Mon. Wea. Rev., 133, 1574–1593, https://doi.org/10.1175/MWR2936.1, 2005.

Anonymous Referee #2

The reviewer comments are formatted in italics and the authors response to the comments are formatted in bold.

Notation *RC2.P#* represents Reviewers Comment. Paragraph Number

RC2.P1 When describing model results, I would suggest to use "present tense" instead of "past tense" throughout the paper.

Response:

Thanks for your kind reminders. In the revised manuscript, we describe the model results in the present tense.

RC2.P2 Line 37: move "in the year 2011" after "Dynamics of the MJO"?

Response:

The modifications are part of "an overview of findings from a multi-nation field campaign called Dynamics of MJO/Cooperative Indian Ocean Experiment on Intraseasonal Variability in the Year 2011 (DYNAMO/CINDY2011)" in the revised manuscript. Please see Page 3, lines 36-39 in the revised manuscript.

RC2.P3 Line 68: may delete "and climate models"

Response:

The revised manuscript removes the wordiness from this sentence. Please see Page 4, line 71 in the revised manuscript.

RC2.P4 Line 109: may change to "regarding the effect of air-sea coupling on the MJO"?

Response:

To make reading easier, we corrected this statement as reviewer's suggestion. Please see Page 6, lines 112-113 in the revised manuscript.

RC2.P5 Line 273-274: Are U850 anomalies not averaged over 10N-10S, instead of just on the equator?

Response:

This was indeed an unclear statement in the original manuscript. These modifications are described as follows: "Figure 2d–f show the time evolution of precipitation and U850 anomalies in Hovmöller diagrams, which represent lagged correlation coefficients between the precipitation averaged over 10°S–5°N, 75–100°E and the precipitation and U850 averaged over 10°N–10°S on intraseasonal timescales". Please see Page 11, lines 251-255 in the revised manuscript.

RC2.P6 In general, figure quality can be improved (many look blur with detals difficult to identify), and some figures can be a bit enlarged.

Response:

Thank you for the suggestions. Figure quality has been improved and size has been enlarged.

RC2.P7 Line 305: the "observed" MJO characteristics

Response:

In response to the suggestion by another reviewer that ERA-Interim reanalysis and NOAA post-processed satellite data (ERA-I/NOAA) should not be referred to as "observation", we have modified the description to "In summary, C–30NS produce coherent and energetic patterns in the eastward-propagating intraseasonal fluctuations of U850 and OLR in the tropical IO and WP that are generally consistent with the MJO characteristics derived from ERA-I and NOAA OLR". Please see Page 12, lines 283-288 in the revised manuscript.

RC2.P8 Line 467: in the first few meters "below the surface" allows ….?

Response:

Thank you for the suggestion. It has been modified to "This result confirms the finding reported by Tseng et al. (2014) that a higher vertical resolution in the upper few meters below the sea surface allows for a faster air–sea interaction, thus resulting in a more realistic simulation of the MJO". Please see Page 19, lines 454-456 in the revised manuscript.

RC2.P9 Line 556: I didn't see faster MJO propagation when the diurnal coupling is turned off based on Fig. 9b. If compared to Fig. 5a, seems to me the MJO propagation speed is even faster in the C-30NS run with diurnal coupling. This is also related to the following comments on Fig. 10. Generally, I don't see significant differences in MJO simulations between the no-diurnal coupling experiment and the control experiment.

Response:

Thank you for the comment. Fig. 9b should be compared with Fig. 2e instead of Fig. 5b. A comparison by eye inspection is not easy to see the difference. Propagation speeds estimated based on the Hovmöller diagrams of U850 and precipitation are shown in Fig. 10. For U850, the MJO with diurnal cycle (marked by target sign) is

faster than the one with no diurnal cycle (marked by Star of David sign). The difference is more evident for U850. We agree that the difference is very small for precipitation. The statement is modified as above in revised manuscript. Please see Page 22, lines 547-550 in the revised manuscript.

RC2.P10 Fig. 10: It would be better provide more details on how the U850 and P slopes are determined, e.g., based on which longitude bands. Also the colors for "C-30NS-nD" are not consistent between the figure and legend.

Response:

In the revised manuscript, we corrected the conflicting colors between the figures and the legend (Fig. RC2.1). Based on the maximum precipitation anomaly and zero values of U850 (indicating deep convection region), propagation speeds of U850 and precipitation are calculated from Hovmöller diagram on intraseasonal timescales between 60°E and 150°W. Please see Page 24, lines 585-588 in the revised manuscript.

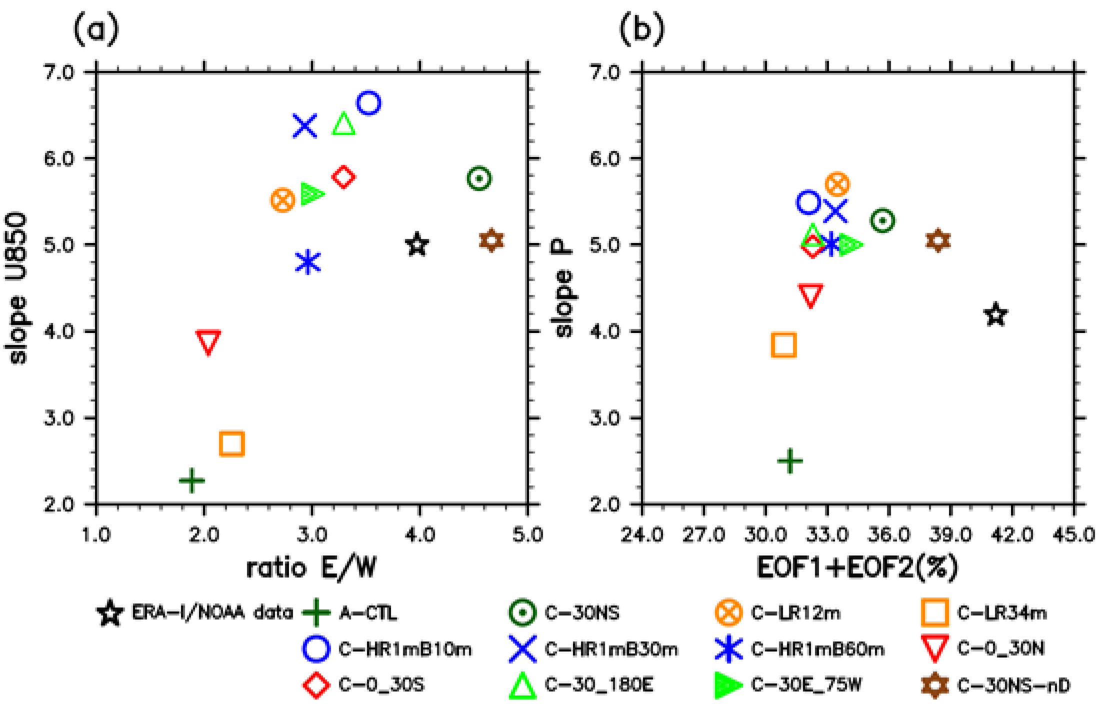

Fig. RC2.1 Scattered plots of various MJO indices in the ERA-I/NOAA data and 12 experiments: (a) power ratio of east/west propagating waves of wavenumber 1–3 of 850-hPa zonal winds (X-axis) with a 30–80-day period and eastward propagation speed of U850 anomaly (Y-axis) from the Hovmöller diagram and (b) RMM1 and RMM2 variance and eastward propagation speed of the filtered precipitation anomaly derived from the Hovmöller diagram.

References:

Tseng, W.-L., Tsuang, B.-J., Keenlyside, N. S., Hsu, H.-H. and Tu, C.-Y.: Resolving the upper-ocean warm layer improves the simulation of the Madden-Julian oscillation, Clim. Dynam., 44, 1487–1503, https://doi.org/10.1007/s00382-014-2315-1, 2014.

Embedding a One-column Ocean Model (SIT 1.06) in the Community Atmosphere Model 5.3 (CAM5.3; CAM5–SIT v1.0) to Improve Madden–Julian Oscillation Simulation in Boreal Winter

Yung-Yao Lan, Huang-Hsiung Hsu*, Wan-Ling Tseng, and Li-Chiang Jiang

Research Center for Environmental Changes, Academia Sinica, Taipei 11529, Taiwan

**Correspondence to*: ~~Yung-Yao Lan (yylan887@gmail.com~~Huang-Hsiung Hsu (hhhsu@gate.sinica.edu.tw)

Abstract

The effect of the air–sea interaction on the Madden–Julian Oscillation (MJO) was investigated using the one-column ocean model Snow–Ice–Thermocline (SIT 1.06) embedded in the Community Atmosphere Model 5.3 (CAM5.3; hereafter CAM5–SIT v1.0). The SIT model with 41 vertical layers was developed to simulate sea surface temperature (SST) and upper-ocean temperature variations with a high vertical resolution that resolves the cool skin and diurnal warm layer and the upper oceanic mixed layer. A series of 30-year sensitivity experiments were conducted in which various model configurations (e.g., coupled versus uncoupled, vertical resolution and depth of the SIT model, coupling domains, and absence of the diurnal cycle) were considered to evaluate the effect of air–sea coupling on MJO simulation. Most of the CAM5–SIT experiments ~~exhibited~~exhibit higher fidelity than the CAM5-alone experiment in characterizing the basic features of the MJO such as spatiotemporal variability and the eastward propagation in boreal winter. The overall MJO simulation performance of CAM5–SIT ~~benefited~~benefits from (1) better resolving the fine vertical structure of upper-ocean temperature and therefore the air–sea interaction that ~~resulted~~result in more realistic intraseasonal variability in both SST and atmospheric circulation and (2) the adequate thickness ~~and vertical resolution~~ of ~~the oceanic~~a vertically-gridded ocean mixed layer. The sensitivity experiments ~~demonstrated~~demonstrate the necessity of coupling the tropical eastern Pacific in addition to the tropical Indian Ocean and the tropical western Pacific. Coupling is more essential in the south than north of the equator in the tropical western Pacific. Enhanced MJO could be obtained without considering the diurnal cycle in coupling.

1. Introduction

The Madden–Julian Oscillation (MJO) is a tropical large-scale convection circulation system that propagates eastward across the warm pool region from the tropical Indian Ocean (IO) to the western Pacific (WP) on an intraseasonal time scale (Madden and Julian, 1972). The MJO is not just an atmospheric phenomenon. The findings ~~of the multination joint~~from a multi-nation field campaign called the Dynamics of MJO/Cooperative Indian Ocean Experiment on Intraseasonal Variability in the Year 2011~~/Dynamics of the MJO (~~ (DYNAMO/CINDY2011; de Szoeke et al., 2017; Johnson and Ciesielski, 2017; Pujiana et al., 2018; Yoneyama et al., 2013; Zhang and Yoneyama, 2017) revealed vigorous air–sea coupling during the evolution of the MJO (Chang et al., 2019; DeMott et al., 2015; Jiang et al., 2015, 2020; Kim et al., 2010; Li et al., 2016; Li et al., 2020; Newman et al., 2009; Pei et al., 2018; Tseng et al., 2014). During the suppression of convection, the MJO propagates eastward with light winds, which is accompanied by enhanced downwelling shortwave radiation absorption, weaker upward latent and sensible fluxes, less cloudiness and precipitation, and weaker vertical mixing in the upper ocean, thus causing an increase in the upper-ocean temperature. In the following active phase when deep convection occurs, downwelling shortwave radiation is reduced and stronger westerly winds enhance ~~evaporation and~~ latent/sensible heat flux (LHF/SHF) loss from the ocean surface, thus causing a decrease in the upper-ocean temperature (DeMott et al., 2015; Madden and Julian, 1972, 1994; Zhang, 2005).

In addition to the ocean surface, the structure of the upper ocean also evolves. Alappattu et al. (2017) reported that during an MJO event, surface flux perturbations cause changes in the ocean thermohaline structure, thus affecting the mixed-layer temperature. The following change in sea surface temperature (SST) can further affect atmospheric circulation of the MJO. Variations in SST mediate ~~heat~~LHF and SHF exchange across the air–sea interface. Although SST responds to atmospheric forcing, ~~its~~the modulation of ~~surface heat fluxes~~LHF and SHF provides feedback to the atmosphere (DeMott et al., 2015; Jiang et al., 2020). Li et al. (2008, 2020) proposed that the phase relationship between SST and convection implies a delayed air–sea interaction mechanism whereby a preceding active-phase MJO may trigger an inactive-phase MJO through the delayed effect of the induced SST anomaly over the IO. The reduction in SST caused by a preceding active-phase MJO may, in turn, ~~yield~~yields delayed ocean feedback that initiates a suppressed-phase MJO, and vice versa. The ~~nonnegligible~~by-no-means negligible effect of intraseasonal SST variations caused by surface heat fluxes suggests that the ocean state can affect the MJO (DeMott et al., 2015, 2019; Hong et al., 2017; Li et al., 2020).

Since its discovery almost five decades ago, the MJO remains a phenomenon that poses a challenge to the capacity of state-of-the-art atmospheric general circulation models (AGCMs) ~~and climate models~~ such as those participating in the Coupled Model Intercomparison Project phase 5 and 6 to generate successful simulations (Ahn et al., 2017, 2020; Bui and Maloney 2018; Jiang et al., 2020; Hung et al., 2013; Kim et al., 2011).

Recent studies have reported that air–sea coupling improves the representation of the MJO in numerical simulation (Bernie et al., 2008; Crueger et al., 2013; DeMott et al., 2015; Li et al., 2016; Li et al., 2020; Tseng et al., 2014; Woolnough et al., 2007). Tseng et al. (2014) indicated that effectively resolving the upper-ocean warm layer to capture temperature variations in the upper few meters of the ocean could improve MJO simulation. DeMott et al. (2015) suggested that the tropical atmosphere–ocean interaction may sustain or amplify the pattern of the enhanced and suppressed atmospheric convection of the eastward propagation. DeMott et al. (2019) demonstrated that the improved MJO eastward propagation in four coupled models resulted from enhanced low-level convective moistening for a rainfall rate of >5 mm day^{-1} due to air–sea coupling. In addition, numerical experiments have been performed to investigate the effect of the diurnal cycle on the MJO (Hagos et al., 2016; Oh et al., 2013), with the results suggesting that the strength and propagation of the MJO through the Maritime Continent (MC) were enhanced when the diurnal cycle was ignored.

Although previous studies have demonstrated the importance of considering the air–sea interaction in a numerical model to improve MJO simulation, additional details regarding model configuration (e.g., vertical resolution~~,~~ and depth of the ocean mixed layer, coupling domain, and absence of the diurnal cycle in air-sea coupling) have not been systematically explored. Tseng et al. (2014) coupled the one-column ocean model Snow–Ice–Thermocline (SIT; Tu and Tsuang, 2005) to the fifth generation of the ECHAM AGCM (ECHAM5–SIT) and indicated that a vertical resolution of 1 m was essential to yield an improved simulation of the MJO with a realistic strength and eastward propagation speed.

In this study, we coupled the SIT model to the Community Atmosphere Model version 5.3 (CAM5.3; Neale et al., 2012)—the atmosphere component of the Community Earth System Model version 1.2.2 (CESM1.2.2; Hurrell et al., 2013)—to explore ~~how~~ the ~~air–sea interaction in AGCMs can improve~~improvement of MJO simulation by coupling SIT model to another AGCM is reproducible in modeling science. The CAM5.3, which has been widely used for the long-term simulation of the climate system, could not efficiently simulate the eastward propagation of the MJO; instead, the model simulated a tendency for the MJO to move westward in the IO (Boyle et al., 2015, Jiang et al, 2015). By contrast, the updated CESM2 with the new CAM6 could realistically simulate the MJO (Ahn et al., 2020; Danabasoglu et al., 2020). Thus, the well-explored CAM5, which does not produce a realistic MJO, appears to be a favorable choice for exploring ~~how~~ coupling a simple one-dimensional (1-D) ocean model, such as the SIT model, can improve MJO simulation, as well as the effects of model configuration~~.~~ on the degree of the improvement. Such a study can also enhance our understanding regarding the effect of air–sea coupling~~'s effect~~ on the MJO.

~~This study examined how air–sea coupling can improve MJO simulation, especially that of the eastward propagation that has been poorly simulated in many climate models.~~ The MJO that exhibits a more substantial eastward propagation in boreal winter than in other seasons was the targeted feature in this study. ~~We~~To examine the sensitivity of MJO simulations to different configurations of air-sea coupling, we conducted a series of 30-year numerical experiments by considering various model configurations (e.g., coupled versus uncoupled, vertical resolution and depth of the SIT model, coupling domains, and absence of the diurnal cycle) to investigate the effect of air–sea coupling. This paper is organized as follows. Section 2 describes the data~~, methodology~~ for validation, the model used for simulation, and ~~model setup. Section 3 presents the~~ the design of ~~coupled model~~numerical experiments. Section ~~4~~3 describes the effect of various ~~model~~air-sea coupling configurations on the MJO simulation determined through detailed MJO diagnostics. ~~A discussion~~Discussion and conclusions are provided in Section ~~5~~4.

~~2.~~ 2. Data, methodology, ~~and~~ model description, and experimental designs

~~2.1 Observational data and analysis methods~~

2.1 Data and methodology

The data analyzed in this study include precipitation from the Global Precipitation Climatology Project~~,~~ (GPCP), outgoing longwave radiation (OLR) and daily SST (Optimum Interpolation SST; OISST) from the National Oceanic and

Atmosphere Administration (NOAA), and parameters from the ERA-Interim (ERA-I) reanalysis (Adler et al., 2003; Dee et al., 2011; Lee et al., 2011; Reynolds and Smith, 1995; Schreck et al., 2018). The ~~initial~~ SST data for the SIT model were obtained from the Hadley Centre Sea Ice and Sea Surface Temperature dataset (Rayner et al., 2003; HadISST1) and the ocean subsurface data (40-layer climatological ocean temperature, salinity, and currents) for nudging were retrieved from the National Centers for Environmental Prediction (NCEP) Global Ocean Data Assimilation System (GODAS; Behringer and Xue, 2004). ~~Ocean bathymetry was derived from the NOAA ETOPO1 data (Amante and Eakins, 2009) and interpolated into 1.9° × 2.5° horizontal resolution.~~

We used the CLIVAR MJO Working Group diagnostics package (CLIVAR, 2009) and a 20–100-day filter (Kaylor, 1977; Wang et al., 2014) to determine intraseasonal variability. MJO phases were defined following the index (namely, RMM1 and RMM2) proposed by Wheeler and Hendon (2004), which considers the first two principal components of the combined near-equatorial OLR and zonal winds at 850 and 200 hPa. The band-passed filtered data were used for calculating the index and defining phases.

2.2 Model description

2.2.1 CAM5.3

The CAM5.3 used in this study has a horizontal resolution of 1.9° latitude × 2.5° longitude and 30 vertical levels with the model top at 0.1 hPa. The MJO could not be realistically simulated in the CAM5.3. Boyle et al. (2015) demonstrated that although making the deep convection dependent on SST improved the simulation of the MJO variance, it exerted a significant negative effect on the mean-state climate of low-level cloud and absorbed shortwave radiation. By comparing the simulation results of an uncoupled and coupled CAM5.3, Li et al. (2016) suggested that air–sea coupling and the convection scheme most significantly affected the MJO simulation in the climate model.

2.2.2 1-D high-resolution TKE ocean model

The 1-D high-resolution turbulence kinetic energy (TKE) ocean model SIT was used to simulate the diurnal fluctuation of SST and surface energy fluxes~~.–~~ (Lan et al., 2010; Tseng et al., 2014; Tu and Tsuang, 2005). The model was well verified against ~~surface and subsurface observations in~~in situ measurements on board the R/V Oceanographic Research Vessel 1 and 3 over the South China Sea (Lan et al., 2010) and on R/V Vickers over the tropical WP (Tu and Tsuang, 2005). ~~Variations in sea water temperature (T), current ($\vec{u}$), and salinity (S) were determined (Gaspar et al., 1990) using the following equations.~~

$$\cancel{\frac{\partial T}{\partial t} = (k_h + \nu_h)\frac{\partial^2 T}{\partial z^2} + \frac{R_{sn}}{\rho_{w0} c_w}\frac{\partial F}{\partial z}} \quad \cancel{(1)}$$

$$\cancel{\frac{\partial \vec{u}}{\partial t} = -f\ \hat{k} \times\ \vec{u} + (k_m + \nu_m)\frac{\partial^2 \vec{u}}{\partial z^2}} \quad \cancel{(2)}$$

$$\cancel{\frac{\partial S}{\partial t} = (k_h + \nu_h)\frac{\partial^2 S}{\partial z^2}} \quad \cancel{(3)}$$

~~where R_{sn} is the net solar radiation at the surface (W m^{-2}), $F(z)$ is the fraction (dimensionless) of R_{sn} that penetrates to the depth z, and k_h and k_m are eddy diffusion coefficients for heat and momentum (m^2 s^{-1}), respectively. The value of k_h within the cool skin layer and that of k_m within the viscous layer were set to zero. Molecular transport is the only mechanism for the vertical diffusion of heat and momentum in the cool skin and viscous layer, respectively (Hasse, 1971; Grassl, 1976; Wu, 1985).The parameters ν_m and ν_h are the molecular diffusion coefficients for momentum and temperature, respectively, ρ_{w0} is the density (kg m^{-3}) of water, and c_w is the specific heat capacity at constant pressure (J kg^{-1} K^{-1}). S is salinity (‰), $\vec{u}$~~

~~is the current velocity (m s^{-1}), f is the Coriolis parameter (dimensionless), and $\hat{k}$ is the vertical unit vector (m s^{-1}).~~

~~The eddy diffusivity for momentum k_m is simulated using an eddy kinetic energy approach based on the Prandtl–Kolmogorov hypothesis as follows:~~

$$k_m = c_k l_k \sqrt{E} \tag{3}$$

~~where $c_k = 0.1$ (Gaspar et al., 1990), l_k is the mixing length (m), and $E = 0.5\left(u'^2 + v'^2 + w'^2\right)$ is turbulent kinetic energy. The turbulent kinetic energy (E) is determined using a 1-D equation (Mellor and Yamada, 1982) as follows:~~

$$\frac{\partial E}{\partial t} = \frac{\partial}{\partial z} k_m \frac{\partial E}{\partial z} + k_m \left(\frac{\partial \vec{u}}{\partial z}\right)^2 + k_h \frac{g}{\rho_w} \frac{\partial \rho_w}{\partial z} - c_\varepsilon \frac{E^{3/2}}{l_\varepsilon} \tag{4}$$

~~where $c_\varepsilon = 0.7$ (Gaspar et al., 1990), g is the gravity (m s^{-2}), ρ_w is the density of water (kg m^{-3}), and l_ε is the characteristic dissipation length (m). The mixing length (l_k) and dissipation length (l_ε) were determined following the approach reported by Gaspar et al. (1990). This approach is valid for determining the eddy diffusivity of both the ocean mixed layer and surface layer.~~

~~In the SIT model setting, the specific heat of sea water is a constant (4186.84 J kg^{-1} K^{-1}), and the Prandtl number in water is defined as the ratio of momentum diffusivity to thermal diffusivity, which is a dimensionless number set as a constant (1.0). The kinematic viscosity is a constant (1.14 × 10^{-6} m^2 s^{-1}; Paulson and Simpson, 1981), and the downward solar radiative flux into water with nine wavelength bands was determined following the approach reported by Paulson and Simpson (1981). The minimum turbulent kinetic energy is set to 10^{-6} m^2 s^{-2}, and the zero displacement is set to 0.03 m.~~

The SIT model determines the vertical profiles of the temperature and momentum of a water column from the surface down to the seabed~~.~~, except in the fixed ocean model bottom experiment. The default setting of vertical discretization (e.g., in the control coupled experiment) is 41 layers with 12 layers in the first 10.5 m, 6 layers between 10.5 m and 107.8 m (Supplementary Information I). In the 1-D TKE ocean model, temperature and salinity below 107.8 m, where vertical mixing is greatly weakened, are nudged toward the climatological values of GODAS data until 4607 m. The extra high vertical resolution is needed to catch detailed temporal variation of upper ocean temperature characterized by the warm layer and cool skin (Tu and Tsuang, 2005). To account for the neglected horizontal advection heat flux, the ocean is weakly nudged (by using a 30-day time scale) between 10.5 m and ~~100~~107.8 m and strongly nudged (by using a 1-day time scale) below ~~100~~107.8 m according to the NCEP GODAS climatological ocean temperature~~; no~~. No nudging is performed ~~for depths under 10 m. Considerably fine 41-layer vertical discretization is applied, with 12 layers in~~within the upper-most 10.5 m. ~~The resolution in the upper 10 m is considerably fine to capture the upper-ocean warm layer, and the thickness of the first layer below sea surface is 0.05 mm to reproduce the ocean surface cool skin. The 41 levels are at the surface and at the depths of 0.05 mm, 1.0 cm, 2.0 cm, 3.0 cm, 4.0 cm, 5.0 cm, 6.0 cm, 7.0 cm, 8.0 cm, 9.0 cm, 10.0 cm, 16.8 cm, 29.5 cm, 43.6 cm, 59.2 cm, 76.9 cm, 96.8 m, 119.4 cm, 145.3 cm, 174.9 cm, 208.9 m, 248.3 cm, 293.8 cm, 346.8 cm, 408.4 cm, 480.2 cm, 564.3 cm, 662.6 cm, 777.9 cm, 913.1 cm, 1072.0 cm, 1258.8 cm, 1478.6 cm, 1737.3 cm, 2042.0 cm, 2401.1 cm, 2824.4 cm, 3323.6 cm, 3912.4 cm, and 4607.1 cm.~~ The SIT model calculates ~~data two times~~twice for each CAM5 time step (30 min; i.e., coupling 48 times per day).

2.3~~.~~ Experimental ~~setup~~design

~~Five sets~~A series of 30-year numerical experiments (Table 1) were conducted to investigate the effect of the air–sea interaction on the MJO simulation. ~~In all simulations,~~The HadSST1 used to force the ~~CAM5.3~~ coupled and uncoupled model was ~~forced by observed~~ the climatological monthly ~~SST except~~ -mean SST averaged over 1982-2001. The monthly SST was linearly interpolated to daily SST fluctuation that forced the model. The SST in ~~the~~air–sea coupling region ~~where the SIT model determined the upper ocean temperature. The~~ was recalculated by the SIT during the simulation, while the prescribed annual cycle of SST was used in the areas outside the coupling region. Ocean bathymetry of the SIT was derived from the NOAA ETOPO1 data (Amante and Eakins, 2009) and interpolated into 1.9° × 2.5° horizontal resolution.

All simulations were driven by the prescribed annual cycle of SST repeatedly for 30 years. The strategy is to evaluate the simulation capacity of climate models under the same condition without considering interannual variation induced by SST. This approach has been widely adopted in many studies (Delworth et al., 2006; Haertel et al., 2020; Subramanian et al., 2011; Tseng et al., 2014; Wang et al., 2005).

Atmospheric initial conditions and external forcing such as CO_2, ozone, and aerosol in near-equilibrium climate state around the year 2000 were taken from F_2000_CAM5 component set based on CESM1.2.2 framework development. The data has been commonly used in present-day simulations using CAM5 (e.g., He et al., 2017).

The setup of five sets of experiment ~~sets were~~ conducted in this study are described as follows.

(1) ~~a~~A standalone CAM5.3 simulation forced by ~~observed~~ climatological monthly ~~SST~~HadISST1 (A–CTL) and ~~a~~the control experiment of coupled CAM5–SIT~~–v1.0~~ simulation (C–30NS; 41 vertical levels, coupling in the entire tropics between 30°~~S~~N and 30°~~N~~S with a diurnal cycle~~);~~).

(2) ~~an upper~~Upper-ocean vertical resolution experiment ~~(C–LR12m and C–LR34m): two coarse vertical resolution simulations with a thickness of 11.8 and 34.2 m, respectively, at the third layer; (3) a lower ocean boundary experiment~~: ~~three~~Two simulations with the ~~lower boundary of the SIT model~~first layer centering at 12 m (C–LR12m) and 34 m (C–LR34m). Further details of the experimental design are shown in supplementary Fig. S1.

(3) Shallow ocean bottom experiment: Three simulations with the ocean model bottom at 10 m (C–HR1mB10m), 30 m (C–HR1mB30m), and 60 m (C–HR1mB60m~~)];~~) (supplementary Fig. S2).

(4) ~~a regional~~Regional coupling experiment: Four simulations with ~~four~~the coupling ~~domains, namely the latitudinal effect [~~region in 0°N–30°N (C–0_30N) and 0°S–30°S (C–0_30S~~)] and the longitudinal~~) for latitudinal effect ~~[~~, and 30°E–180°E (C–30_180E) and 30°E–75°W (C–30E_75W~~)] (see the~~) for longitudinal effect. The coupling ~~domain~~domains are shown in Fig. 1~~); and~~ .

(5) ~~a~~ A non-diurnal ~~coupling experiment: a nondiurnal~~ simulation (C–30NS–nD) that considers the air–sea interaction ~~by~~ only once a day, namely, calculating ~~ocean-surface fluxes~~ SHF and LHF based on daily mean atmospheric variables and SST ~~(C–30NS–nD), with~~. To prevent the inconsistent local time in different regions, the coupling frequency ~~maintained~~at each grid point remained 48 times per day ~~to prevent the local time in different regions from being inconsistent when coupling once a day. Greenhouse gas concentrations were fixed at the~~ using the same daily means of atmospheric variables and SST at that particular point. In contrast, the control simulation calculates air-sea fluxes 48 times a day based on instantons values ~~observed in the year 2000~~. A comparison between the non-diurnal simulation and the control simulation reveals the effect of diurnal cycle in air0sea coupling.

~~The main codes of the SIT model in Fortran 90 are packaging in independent and original subprograms, with data and interface blocks in modules, that creates explicit interfaces between the CAM5.3 and the SIT model without a coupler. In addition, these modules contain dynamically allocable arrays and the independent I/O procedures of the SIT model. The coupler in the CAM5 SIT only brokers communication interchanges between the simulated SST and calculated oceanic surface fluxes.~~

4

3. Results and Discussion

The realistic simulation of the MJO has always been a major bottleneck in the development of climate models. In this section, we demonstrate ~~how~~the sensitivity of air–sea coupling experiments using a 1-D high-resolution ocean~~ mixed-layer~~ model significantly improves the MJO simulation by the CAM5.3. The period between November and April when the MJO is the most prominent was the targeted season in this study.

43.1 Improvement of MJO simulation through air–sea coupling

This subsection compares the MJO simulation of the control coupled ~~model~~experiment (C–30NS) with that of the uncoupled AGCM (A–CTL) forced by climatological monthly SST of HadISST1 to demonstrate the effect of air–sea coupling on the MJO simulation by coupling the SIT model to the CAM5.3 in the tropical belt (30°N–30°S).

43.1.1 Wavenumber–frequency spectra and eastward propagation characteristics

A wavenumber–frequency spectrum (W–FS) analysis was conducted to quantify propagation characteristics simulated in different experiments. The spectra of unfiltered U850 in ~~observation~~ERA-I reanalysis, C–30NS, and A–CTL are shown in Fig. 2a–c, respectively. The ~~coupled~~ C–30NS ~~effectively simulated~~considering the ~~observed~~coupling in 30ºN–30ºS realistically simulates eastward-propagating signals at zonal wavenumber 1 and 30–80-day periods (Fig. 2a–b), although with a slightly larger amplitude~~.~~ compared with ERA-I. By contrast, the uncoupled A–CTL ~~did~~does not ~~effectively simulate the observed characteristics~~yield realistic simulation; instead, it ~~simulated~~simulates both eastward (wavenumber 1)- and westward (wavenumber 2)-propagating signals with an unrealistic spectral shift to time scales longer than ~~the observed~~ 30–80-day ~~period~~.

The major features of the simulated MJO propagation were examined. Figure 2d–f show the time evolution of ~~intraseasonal~~ precipitation and U850 anomalies in Hovmöller diagrams~~; specifically,~~, which represent lagged correlation coefficients between the precipitation ~~at~~averaged over 10°S–5°N, 75–100°E ~~with~~and the ~~average~~ precipitation ~~at~~and U850 averaged over 10°N–10°S ~~and U850 anomalies along the equator~~on intraseasonal timescales. Figure 2d indicates eastward propagation for both precipitation and U850 from the eastern IO to the dateline, with precipitation leading U850 by approximately a quarter of a cycle. The Hovmöller diagram derived from the C–30NS (Fig. 2e) exhibits the key characteristics of eastward propagation for both precipitation and U850 and the relative phases between the two, although the simulated correlation ~~was~~is slightly weaker than that ~~observed.~~derived from GPCP and ERA-I. By contrast, the uncoupled A–CTL ~~simulated~~simulates intraseasonal signals that ~~propagated~~propagate westward over the IO and ~~simulated~~ weak and much slower eastward propagation crossing the MC and WP (Fig. 2f). The contrast between Fig. 2e and 2f ~~demonstrated~~demonstrate that coupling a 1-D ~~ocean~~ TKE ocean model alone could lead to a significant improvement in an AGCM in simulating the major characteristics (e.g., amplitude, propagation direction and speed, and phase relationship between precipitation and circulation) of the MJO.

~~4~~3.1.2 Coherence of the simulated MJO

Cross-spectral analysis was ~~performed~~conducted to examine the coherence and phase lag between tropical circulation and convection, which were plotted over the tropical wave spectra. Figure 2g–i show the symmetric part (e.g., Wheeler and Kiladis, 1999) of OLR and U850 in ~~observation~~ERA-I/NOAA data, C–30NS, and A–CTL, respectively. We present only ~~a magnified display of~~ the spectra between ~~the frequency of~~ 0 to 0.35 day^{-1} to highlight the MJO and equatorial Kelvin waves. The most prominent ~~characteristic observed was~~characteristics seen in ERA-I/NOAA data are the peak coherence at wavenumbers 1–3 and a phase lag of approximately 90° in the 30–80-day band ~~for the symmetric component associated with the MJO~~ (Ren et al., 2019; Wheeler and Kiladis 1999). The coupled experiment C–30NS ~~simulated~~simulates strong coherence in this low-frequency band (wavenumber 1) and ~~exhibited~~exhibits a realistic phase lag relationship between U850 and OLR perturbations. However, the coherence at wavenumbers 2–3 for the 30–80-day period simulated by C–30NS ~~was~~is weaker than that ~~observed. In addition, this~~in ERA-I/NOAA data. This undersimulation was also noted in CCSM4 (Subramanian et al., 2011), the uncoupled and coupled CAM4 and CAM5 (Li et al., 2016), and NorESM1-M (Bentsen et al., 2013), which had a version of the CAM as an AGCM. In summary, C–30NS ~~produced~~considering the coupling between 30ºN–30ºS produces coherent and energetic patterns in the eastward-propagating intraseasonal fluctuations of U850 and OLR in the tropical IO and WP that are generally consistent with the MJO characteristics. By contrast, the MJO characteristics in A–CTL ~~were~~are considerably weaker than those in C–30NS and that ~~observed~~in ERA-I/NOAA data.

~~4~~3.1.3 Horizontal and vertical structures of the MJO across the MC

Figure 2j–o show the horizontal and vertical structures of the MJO when deep convection is the strongest over the MC (i.e., phase 5). Figure 2j–l present the 20–100-day filtered OLR (W m^{-2}, shaded) and 850-hPa wind (m s^{-1}, vector). C–30NS realistically simulated the enhanced tropical convection over the eastern IO and the Kelvin-wave-like easterly anomalies over the tropical WP despite undersimulating the convection over the MC (Fig. 2j and 2k). By contrast, A–CTL failed to simulate the enhanced convection over the eastern IO and MC; instead, it simulated considerably weaker convection and easterly winds over the MC and WP, respectively, than that ~~observed~~in ERA-I/NOAA data (Fig. 2j and 2l).

Figure 2m–o show the vertical–longitudinal profiles of 20–100-day filtered 15°N–15°S averaged vertical velocity (OMEGA; Pa s^{-1}, shaded) and moist static energy (MSE) anomalies (W m^{-2}, contour) at phase 5. The spatial distribution of negative OMEGA (ascending motion) anomalies generally agreed with OLR anomalies in C–30NS simulation and ~~observation~~NOAA data over the Indo-Pacific region (Fig. 2m and 2n). The ~~observed relative~~relatively spatial relationship between the ascending motion and MSE ~~was~~seen in ERA-I is well simulated in the coupled experiment C–30NS. For example, positive MSE anomalies on the eastern side of the anomalous ascent ~~demonstrated~~demonstrate that the energy recharge process occurs in advance of the MJO convection over the lower-tropospheric easterlies (Fig. ~~2j~~2m and ~~2k~~2n), whereas negative MSE anomalies on the western side ~~revealed~~reveal that the discharge process occurs during and after convection over the lower-tropospheric westerlies. By contrast, this phase relationship, considered to be an essential feature leading to the eastward propagation of an MJO (Hannah and Maloney 2014; Heath et al., 2021), ~~was~~is not properly simulated in the uncoupled experiment A–CTL (Fig.

2o), in which the simulated weak negative OMEGA ~~was~~is located between negative and positive MSE anomalies over weak lower-tropospheric wind anomalies and associated with weak convection over the MC (Fig. 2l).

The ~~observed~~ temporal evolution of NOAA OLR and ERA-I U850 (Fig. 3a) ~~indicated~~indicates that convection originating in the western IO ~~was~~is enhanced during its eastward propagation to the MC where it ~~reached~~reaches the peak amplitude and then gradually weakened when continuing moving eastward to the dateline. ~~In~~In the coupled experiment C–30NS, this evolution of convectively coupled circulation ~~was~~is realistically simulated, although it ~~was~~is weaker than the ~~observed~~ strength seen in NOAA OLR (Fig. 3b). Moreover, the split of convection into two cells off the equator in phase 6 ~~was~~is appropriately simulated in C–30NS (P6 in Fig. 3a and 3b). This split was caused by the topographic and land–sea contrast effects of the MC (Tseng et al., 2017). Associated with the split ~~was~~is the southward detouring of the anomalous convection during the passage of the MJO through the MC (Kim et al. 2017, Tseng et al., 2017; Wu and Hsu, 2009). After the passage of the MJO through the MC, the anomalous convection ~~stayed~~stays south of the equator and ~~continued~~continues moving eastward to the dateline. In the uncoupled A–CTL, the systematic eastward propagation of convectively coupled MJO circulation from the IO into the MC ~~was~~is not simulated. Instead, the convection over the MC ~~developed~~develops in situ at a later stage than that observed (e.g., P6 in Fig. 3c) and dissipated rapidly. The A–CTL ~~simulated~~simulates a pair of off-equator convection anomalies in the eastern IO during phase 2 (P2 in Fig. 3c) that ~~moved~~moves westward toward the central IO and were amplified at later stages (e.g., P4 in Fig. 3c). This unrealistic evolution explains the westward propagation tendency observed in the Hovmöller diagram (Fig. 2f).

~~4~~3.1.4 Characteristics of air–sea interaction

Figure 4a–c show the longitude–phase diagram in which the 20–100-day filtered precipitation (shaded) and SST (contour) anomalies were averaged over 10°S–10°N to determine the relationship between precipitation and SST fluctuations and to establish a link between air–sea coupling and convection. The propagation of the enhanced convection with positive SST anomalies to the east could be clearly seen in ~~observation~~GPCP/OISST and the coupled experiment C–30NS (Fig. 4a and 4b). The highest SST anomaly (SSTA) ~~led~~leads the maximum precipitation anomaly by approximately 2–3 phases, and the SSTA ~~began~~begins to decrease following the onset of enhanced precipitation. The ~~observation revealed~~ERA-I and OISST data reveal the following relationship between net surface flux and SST: the decreased (increased) ~~latent/sensible heat fluxes~~LHF/SHF and increased (decreased) downward radiation flux leading (lagging) the positive (negative) SSTA east (west) of anomalous deep convection. This well-known lead–lag relationship reflecting the active air–sea interaction in an MJO ~~was~~is realistically simulated in the coupled experiment C–30NS (not shown).

The contrast between C–30NS and A–CTL confirms the key role of the air–sea interaction in contributing to the eastward propagation and demonstrates that the eastward propagation simulation can be markedly improved by incorporating the air–sea interaction process in the model, even when using a simple 1-D ocean model such as SIT.

~~4~~3.1.5 Vertically tilting structure

The warm SST was the key forcing that contributed to the boundary layer convergence before the onset of deep convection (Li et al., 2020; Tseng et al., 2014). Hence, the warmer upper ocean enhances the low-level atmospheric convergence and then leads to enhanced low-level moisture and preconditioned deep convection and eastward propagation. This moistening process associated with warm ocean surface temperature ~~was~~is well simulated in the coupled experiment C–30NS but is not shown here. Instead, we present the coupling of moisture divergence (MD) and atmospheric circulation.

MD and zonal wind anomalies from the surface to the upper troposphere averaged over the 10°S–10°N and 120–150°E region are shown in Fig. 4d–f to depict the relationship between the vertically tilting structure of MD and zonal wind anomalies. Note that the active convection occurred around phase 5. The coupled experiment C–30NS (Fig. 4e) realistically ~~simulated~~simulates the ~~observed~~ deepening of coupled MD and zonal wind anomalies with time (Fig. 4d). An evolution from the right to left seen in each panel of Fig. 4d–f ~~was~~is equivalent to the eastward movement of vertically tilting circulation from the eastern IO into the MC because of the eastward-propagating nature of the MJO. Figure 4d and 4e show that in both ~~observation and~~ERA-I reanalysis and the coupled experiment C–30NS, the near-surface convergence (negative MD) occurring in the easterly anomalies ~~led~~lead the convection and continued deepening up to 500 hPa from phase 2 to phase 6 when the easterly anomalies ~~switched~~switch to westerly anomalies. By contrast, this ~~observed~~ evolution of coupled MD–zonal wind anomalies ~~were~~are not appropriately simulated in the uncoupled experiment (Fig. 4f). For example, a slow deepening with time ~~was~~is observed in the MD anomaly but not in the zonal wind anomaly that ~~exhibited~~exhibits a vertically decayed structure, suggesting that MD and wind anomalies ~~were~~are not well coupled, as noted in ~~observation~~the ERA-I/NOAA data and the control coupled experiment.

In ~~observation~~the ERA-I reanalysis data, the negative near-surface MD anomalies ~~appeared~~appear first under the easterly anomaly and ~~continued~~continue deepening between the easterly and westerly anomalies. This development in the phase relationship between MD and zonal wind anomalies in both ~~observation~~ERA-I reanalysis data and the coupled simulation is consistent with the well-known structure embedded in the MJO, namely the near-surface convergence in the easterly phase (i.e., a boundary-layer moistening process; Kiranmayi and Maloney 2011; Li et al., 2020; Tseng et al., 2014), followed by the deep convection when transitioning to the westerly phase. This close phase relationship that is key to the eastward propagation ~~was~~is appropriately simulated in the coupled experiment but not in the uncoupled experiment.

~~4~~3.1.6 Intraseasonal variance of precipitation

Figure 4g–i present the spatial distribution of intraseasonal variance of precipitation. In ~~observation~~the GPCP data, the maximum variance ~~was~~is noted over the tropical eastern IO, MC, and tropical WP. The maximum variance south of the island in the MC and the equator in the tropical WP reflects the southward shift of the MJO deep convection when passing through the MC, partly due to the blocking effect of mountainous islands and the higher moisture content over high SST south of the equator in the region during boreal winter (Kim et al., 2017; Ling et al., 2019; Sobel et al., 2008; Tseng et al., 2017; Wu and Hsu, 2009). Although the control coupled experiment ~~failed~~fails to simulate the variance maximum in the tropical eastern IO, it appropriately ~~simulated~~simulates the maximum variance over the tropical WP, reflecting its ability to simulate the eastward propagation of the MJO through the MC. By contrast, the uncoupled A–CTL experiment ~~simulated~~simulates considerably weaker intraseasonal variance in both the tropical eastern IO and the tropical WP. Figure 4j–l are the 20–100-day filtered SST (K, shaded) and 850-hPa wind (m s^{-1}, vector) during MJO phase 7 when deep convection is the strongest over the dateline.

The coupled experiment C–30NS realistically ~~simulated~~simulates the negative SST anomaly over the MC and WP when enhanced tropical convection passed through the MC to the dateline, indicating the capability of the SIT model to reproduce the ~~observed~~ SST anomaly by exchanging ~~surface fluxes~~LHF/SHF between the atmosphere and ocean. In A-CTL, no SST anomaly ~~was~~is evident because the model was forced by prescribed climatological SST. The contrast seen in Fig. 4j–l demonstrates the essential role of atmosphere–ocean coupling in shaping the MJO. A delayed air–sea interaction mechanism was noted, where a preceding active-phase MJO may trigger an inactive-phase MJO through the delayed effect of the induced SST anomaly. In addition, the westerly winds at 850 hPa moving southward between MC and WP ~~were~~are captured by the control experiment C–30NS and ~~were~~are similar to the ~~observed~~ERA-I reanalysis winds (Fig. 4j and 4k). By contrast, A–CTL forced by climatological monthly SST (<0.05 K phase^{-1} anomaly) ~~failed~~fails to simulate the southward westerly wind of the region extending from the MC to the dateline (Fig. 4l).

~~4.2~~3.2 Effect of upper-ocean vertical resolution

In the control coupled experiment C–30NS, the vertical resolution in the upper 10.5 m was 1 m. Tseng et al. (2014) suggested that fine vertical resolution is crucial for appropriately simulating the eastward propagation. To investigate the effect of vertical resolution, two ~~coarse-resolution~~ experiments with a thicker first layer were conducted~~, which involved increasing~~ by moving the ~~thickness~~center of the ~~first ocean layer (under the cool skin~~ layer~~)~~ to 11.~~8~~5 m (C–LR12m) and ~~34.2~~33.9 m (C–LR34m), respectively~~.~~, as opposed to the control experiment in which 10 layers were implemented in the first 10.5 meters (see supplementary Fig. S1 for vertical discretization). The W–FS spectral peaks of U850 in C–LR12m ~~were~~are concentrated in eastward-propagating wavenumber 1 at three timescales (e.g., longer than 80 days, 30–80 days, and approximately 30 days; Fig. 5a). In C–LR34m, both eastward and westward signals ~~were~~are simulated with the dominant W–FS timescale~~ that was~~ longer than 80 days (Fig. 5b). The appearance of both eastward and westward signals at a lower frequency implied a stronger stationary tendency or weaker eastward-propagating tendency. This result is consistent with that reported by Tseng et al. (2014) that the scientific reproducibility of coarser ~~the~~ resolution ~~is, the~~causes a longer intraseasonal periodicity and slower~~ is the~~ eastward propagation of the MJO.

The effect of vertical resolution on the MJO simulation can be seen in the Hovmöller diagram. The eastward propagation simulated in C–LR12m (Fig. 5c) markedly weakened after crossing the MC ~~compared~~compare with that simulated in the control experiment C–30NS~~.~~ (Fig. 2e). In C–LR34m, the quasi-stationary fluctuation and westward propagation ~~were~~are simulated over the IO (Fig. 5d), appearing similar to those in A–CTL~~.~~ (Fig. 2f). The~~ observed~~ lead–lag relationship between precipitation (zonal wind) and SST ~~was~~is poorly simulated in C–LR12m (Fig. 5e) and even more poorly simulated in C–LR34m (Fig. 5f). This result confirms the finding reported by Tseng et al. (2014) that a higher vertical resolution in the ~~first~~upper few meters below the surface allows for a faster air–sea interaction, thus resulting in a more realistic simulation of the MJO.

~~4~~3.3 Effect of the lowest boundary of the SIT model

The ocean is a vital energy source for the MJO. Although vertical resolution is crucial for the efficiency of air–sea interaction, the thickness of the upper ocean that interacts with the atmosphere represents the ocean heat content to substantiate the MJO. A key question is how thick ~~an oceanic~~a vertically-gridded ocean mixed layer should be for a realistic simulation. To explore this issue, three experiments with a model ocean with a 1-m vertical resolution and the ocean model (SIT) bottom at 10, 30, and 60 m, which included the top ~~11, 13~~12, 14, and ~~15~~16 levels, respectively, as ~~listed~~shown in ~~Section 2~~supplementary Fig. S2 and Table 1, were conducted. The spectra and the Hovmöller diagrams shown in Fig. 6a–c and Fig. 6d–f, respectively, demonstrate that the thicker ocean model ~~ocean simulated~~simulates a stronger MJO with a frequency closer to those in the ~~observation and an~~coupled experiment C–30NS and ERA-I/NOAA data, and more realistic eastward propagation ~~similar to that in C–30NS and observations.~~. In addition, the lead–lag relationship between precipitation (wind) and SST ~~was~~is more realistically simulated with increasing thickness of the ocean model (Fig. 6g–i).

This result suggests that the thickness of the ~~upper ocean~~oceanic mixed layer that interacts with the atmosphere strongly affects the frequency of the simulated MJO. A thinner (thicker) oceanic mixed layer is more quickly (slowly) recharged and discharged through ~~heat~~SHF and LHF exchange between the atmosphere and ocean and therefore likely fluctuates at a faster (slower) tempo. The simulated periodicity is therefore affected by the thickness of oceanic mixed layer (or ocean heat content). Although ~~this study~~the result suggests 60 m is an appropriate thickness to realistically simulate the periodicity of the MJO, we did not intend to suggest the exact thickness required for a proper simulation because it might depend on the model. The oceanic mixed layer should be adequately thick to contain a certain amount of heat to generate appropriate periodicity ~~that is close to that observed~~. However, the reason for the intraseasonal time scale (i.e., 20-100 days) should be determined in future studies. This finding does not suggest a constant periodicity because periodicity might be affected by the time-varying structure of the atmosphere and ocean in the real world.

~~4~~3.4 Effects of coupling domains

The MJO is a planetary-scale phenomenon. Given its large-scale circulation, the air–sea interaction affecting the MJO likely occurs in a much larger area than the region near the major convection anomalies. In this section, we discuss ~~whether and how~~ the effect of coupling domain ~~affects a~~on model~~'s~~ ability to simulate the eastward propagation speed and periodicity of the MJO. Four experiments considering the coupling in various domains (C–0_30N, C–0_30S, C–30_180E, and C–30E_75W, Fig. 1) were conducted ~~to investigate~~for the ~~effect of the coupling domain on the eastward propagation speed and periodicity of the MJO in the simulation.~~purpose. The results are shown in Fig. 7. ~~The domains of the four experiments are shown in Fig. 1.~~ The C–0_30N that considered the coupling in the tropics between the equator and 30°N ~~simulated~~simulates the least realistic MJO propagation in terms of W–FS (Fig. 7a), zonal wind–precipitation coupling (Fig. 7e), and SST–precipitation (Fig. 7i) ~~of~~among the four regional coupling experiments. By contrast, coupling only the tropics between the equator and 30°S ~~simulated~~simulates a more realistic MJO in all three aspects (i.e., spectrum in Fig. 7b, temporal evolution of precipitation/wind, and precipitation/SST coupling in Fig. 7f and 7j). Figure. 8a indicates that the ~~positive precipitation~~negative OLR anomalies at phase 5 simulated in C–0_30N ~~stayed~~stays mainly north of the equator and ~~did~~does not shift southward in the MC as ~~observed~~revealed in ERA-I reanalysis and ~~in~~NOAA OLR and in the control experiment C–30NS, and the convection over the IO ~~was~~is unrealistically weak. By contrast, the southward detouring in the MC ~~was~~is realistically simulated in C–0_30S that coupled only the tropical ocean between the equator and 30°S. This result indicates that air–sea coupling occurring south of the equator is the key to producing appropriate eastward propagation and detouring of the MJO through the MC. Without this coupling, the C–0_30N experiment ~~failed~~fails to realistically simulate the eastward propagation of the MJO~~.~~ (Fig. 7e). This contrast can be attributed to the

~~observed~~ warmer ocean surface and higher moisture content found south of the equator in boreal winter, which comprise a more favorable environmental condition for air–sea coupling and convection–circulation coupling and the occurrence of the MJO.

MJO simulations can be affected by air–sea coupling in the longitudinal domain. Tseng et al. (2014) examined this effect by allowing coupling in different regions (e.g., the IO, WP, and IO + WP) and found that the IO + WP coupling experiment yielded the most satisfactory MJO simulation in terms of the zonal W–FS and eastward propagation characteristics. In this study, we conducted sensitivity experiments in which we allowed coupling in the tropics in two longitudinal domains, namely 30°E–180°E (C–30_180E) and 30°E–75°W (C–30E_75W). The 30°E–180°E region covered the IO and WP, and the 30°E–75°W region covered the IO and the entire tropical Pacific. As shown in Fig. 7, the C–30E_75W experiment ~~simulated the MJO, yielding results~~simulates more ~~similar to the observation and those in C-30NS~~realistic MJO than ~~to~~the C–30_180E experiment, with stronger eastward propagation and larger amplitudes in the spectrum (Fig. 7c and 7d) and Hovmöller diagrams of precipitation/wind (Fig. 7g and 7h) and precipitation/SST (Fig. 7k and 7l). The simulated MJO in C–30E_75W propagated ~~further~~farther east than that in C–30_180E, particularly evident in Fig. 7k and 7l. The spatial distributions of circulation and ~~precipitation~~OLR shown in Fig. 8c and 8d ~~indicated~~indicate the presence of a stronger convective-coupled circulation system over the MC and WP in C–30E_75W. These results suggest that coupling over the entire tropical IO and Pacific could enhance the strength and eastward propagation of the MJO and encourage ~~further~~farther propagation to the central Pacific.

~~4~~3.5 Diurnal versus no diurnal cycle in air–sea coupling

~~The~~Previous studies showed that the diurnal cycle in the MC can weaken the MJO and its eastward propagation (Hagos et al., 2016; Oh et al., 2013). We conducted an experiment to determine whether ~~the~~computing surface heat fluxes using daily mean ~~value~~values, instead of instantaneous values, of atmospheric variables and SST with the same coupling frequency would affect the MJO simulation. The coupling in the model was ~~performed~~conducted through ~~heat flux~~the SHF and LHF exchange between the atmosphere and ocean~~.~~, that were calculated based on simulated winds, moisture, and temperature. As mentioned in Section 2.3, air–sea fluxes were calculated twice for every time step (coupling 48 times per day~~,~~) in the control coupled experiment (C–30NS) based on the instantaneous values of atmospheric and oceanic variables. In the experiment in which the diurnal cycle was removed (C–30NS–nD), air–sea fluxes were calculated as in C–30NS but were based on daily ~~mean data.~~means of both atmospheric variables and SST. Doing this removed certain diurnal effects of air-sea coupling. The results shown in Fig. 9 reveal the enhancement of the eastward-propagating signals in the MJO (e.g., a larger amplitude in spectrum; Fig. 9a) and further eastward ~~and faster~~ propagation (Fig. 9b) as well stronger coupling between precipitation and SST (Fig. 9c~~).~~) in C–30NS–nD. The overall results are consistent with previous finding that the diurnal cycle tends to reduce the amplitude ~~and propagation~~ of the MJO, indicating that the weakening effect occurs through air–sea coupling in addition to those processes in the atmosphere. Previous studies have hypothesized that rapid interaction processes in the diurnal time scale tend to extract energy from the MJO, thus reducing ~~both~~ the strength and propagation tendency of the MJO. However, a comparison between the spectra of C–30NS and C–30NS–nD ~~indicated~~indicates that the experiment in which the diurnal cycle ~~was~~is removed appeared to oversimulate the MJO with unrealistic strength, suggesting that the effect of the diurnal cycle should be considered in the model to simulate a more realistic MJO. However, whether this is a common result in different models remain to be examined.

~~5~~ 4. Discussion and conclusions

Air–sea coupling is a key mechanism for the successful simulation of the MJO (Chang et al., 2019; DeMott et al., 2015; Jiang et al., 2015, 2020; Kim et al., 2010; Li et al., 2016; Li et al., 2020; Newman et al., 2009; Tseng et al., 2014). This study, following the study ~~conducted by~~of Tseng et al. (2014), demonstrated that coupling a high-resolution 1-D TKE ocean model (namely the SIT model) to the CAM5, namely the CAM5–SIT, significantly improved the MJO simulation over the standalone CAM5. ~~The CAM5–SIT realistically simulated~~By coupling SIT model to an AGCM different from Tseng et al. (2014), this study confirms the scientific reproducibility for the improvement of MJO simulation in modeling science. The CAM5–SIT realistically simulates the MJO characteristics in many aspects (e.g., intraseasonal periodicity, eastward propagation, coherence in the low-frequency band, detouring propagation across the MC, tilting vertical structure, and intraseasonal variance in the WP).

Systematic sensitivity experiments were conducted to investigate the effects of the vertical resolution and the thickness of the 1-D ocean model, coupling domains, and the absence of the diurnal cycle. The results of all the sensitivity experiments are summarized in Fig. 10a and 10b, which show four common metrics for MJO evaluation. The four metrics are the propagation speed of the MJO (estimated from the U850 Hovmöller diagram as Fig. 2d–f) versus the power ratio of eastward- and westward-propagating 30–80-day signals (E/W ratio, derived from the zonal W–FS) in Fig. 10a– and the eastward propagation speed of the 30–80-day filtered precipitation anomaly (estimated from the precipitation Hovmöller diagram) versus the variance explained by RMM1 and RMM2 (i.e., the sum of the variance explained by EOF1 and EOF2 based on Wheeler and Hendon, 2004) in Fig. 10b. Based on the maximum precipitation anomaly and zero values of U850 (indicating deep convection region), propagation speeds of precipitation and U850 were calculated from Hovmöller diagrams between 60°E and 150°W. Overall, the control experiment C–30NS simulates the most realistic MJO among all sensitivity experiments.

As for vertical resolution, we determined that the MJO simulation efficiency decreased when the vertical resolution of the SIT model ~~was~~is decreased from 1 m to 12 or 34 m, as ~~observed~~simulated in the C–LR12m and C–LR34m experiments, respectively. This finding, consistent with that reported by Tseng et al. (2014), suggests that a finer vertical resolution more effectively resolves temperature variations in the ocean warm layer and enhances atmospheric–ocean coupling, thus enabling the upper ocean to more efficiently respond to atmospheric forcing by providing sensible and latent heat fluxes; this results in superior synchronization between the lower atmosphere and the upper ocean.

We observed that the ~~thinner~~shallower ocean ~~mixed layer~~model bottom could speed up the eastward propagation of the MJO by producing more perturbations of shorter periodicity (Fig. 6) and ~~resulted~~results in a weaker MJO. The shallower oceanic mixed layer likely ~~responded~~responds more quickly to atmospheric forcing but ~~provided~~provides less sensible and latent heat fluxes to the atmosphere. Thus, the MJO ~~propagated~~propagates too fast with a weaker amplitude.

In the coupling domain sensitivity experiments, we investigated the essential coupling domain required to simulate the realistic MJO and the effect of the domain on the MJO simulation. Coupling only the northern tropics ~~failed~~fails to simulate the eastward propagation, whereas coupling only the southern tropics ~~yielded~~yields a more realistic MJO simulation, although this simulation ~~was~~is inferior to coupling the entire tropics. This contrast reveals the importance of the southern tropical ocean, especially in the MC where high SST and moisture content are noted. Coupling in the southern tropics is therefore essential for providing the energy required to maintain the MJO and its eastward propagation. By contrast, the northern tropics are relatively dry and cool. Coupling in this region is therefore less effective in improving MJO simulation.

In the longitudinal domain sensitivity experiments, we found that the MJO amplitude and the eastward extend of its eastward propagation ~~were~~are enhanced by extending the eastern boundary of the coupling domain from the tropical eastern IO to the tropical WP and further to the tropical eastern Pacific (Fig. 1). Further extension of the domain to cover the tropical Atlantic ~~did~~does not exhibit further enhancement (not shown). This result indicates that coupling in the tropical central and eastern Pacific, although not the major MJO signal regions (i.e., from the tropical IO to the tropical WP), still played a marked role in sustaining the MJO. We propose the following to explain this effect. Because of the planetary scale of the MJO, the near-surface easterly circulation to the east of the convection core often extended to the tropical central and eastern Pacific where the climatological easterly prevailed. The coupling beyond the WP increased low-level moisture transport and convergence to the east of the convection and establish an environment suitable for the further eastward propagation of the MJO. This effect was likely terminated by the landmass of Central America when the tropical Atlantic was further included. Thus, a further eastward extension of the coupling domain exerted little effect on further enhancing the MJO. A diagnostic study on the effect of the longitudinal coupling domain is being conducted, and the results will be reported in a following paper.

The diurnal versus nondiurnal cycle experiment ~~indicated~~indicates that nondiurnal coupling tended to enhance eastward-propagating signals but slow down the eastward propagation~~.~~ (Fig. 10a–b). This result is consistent with the finding of previous studies that the diurnal cycle in the atmosphere extracts energy from the MJO, thus weakening it.

In this study, we demonstrated how air–sea coupling can improve the MJO simulation in a GCM. The findings are as follows.

(1) Better resolving the fine structure of the upper-ocean temperature and therefore the air–sea interaction ~~led~~leads to more realistic intraseasonal variability in both SST and atmospheric circulation.

(2) An adequate thickness of the oceanic mixed layer is required to simulate a delayed response of the upper ocean to atmospheric forcing and lower-frequency fluctuation.

(3) Coupling the tropical eastern Pacific, in addition to the tropical IO and the tropical WP, can enhance the MJO and facilitate the further eastward propagation of the MJO to the dateline.

(4) Coupling the southern tropical ocean, instead of the norther tropical ocean, is essential for simulating a realistic MJO.

(5) Stronger MJO variability can be obtained without considering the diurnal cycle in coupling.

Our study confirmed the effectiveness of air–sea coupling for improving MJO simulation in a climate model and demonstrated how and where to couple. The findings enhance our understanding of the physical processes that shape the characteristics of the MJO.

Code and data availability. The model code of CAM5–SIT is available at https://doi.org/10.5281/zenodo.5510795. Input data of CAM5–SIT using the climatological Hadley Centre Sea Ice and Sea Surface Temperature dataset and GODAS data forcing, including 30-year numerical experiments, are available at https://doi.org/10.5281/zenodo.5510795.

Author contributions. HHH is the initiator and the primary investigator of the Taiwan Earth System Model project. YYL is the CAM5–SIT model developer and writes the majority part of the paper. WLT and LCJ assist in MJO analysis.

Competing interests. The authors declare that they have no conflict of interest.

Acknowledgements. The contribution from YYL, HHH, WLT, and LCJ to this study is supported by Ministry of Science and Technology of Taiwan under contracts MOST 110-2123-M-001-003, MOST 110-2811-M-001-603, MOST 109-2811-M-001-624 and MOST108-2811-M-001-643. Our deepest gratitude goes to the editors and anonymous reviewers for their careful work and thoughtful suggestions that have helped improve this paper substantially. We sincerely thank the National Center for Atmospheric Research and their Atmosphere Model Working Group (AMWG) for release CESM1.2.2. We thank the computational support from National Center for High530 performance Computing of Taiwan. This manuscript was edited by Wallace Academic Editing.

Reference

Adler, R. F., Huffman, G. J., Chang, A., Ferraro, R., Xie, P. P., Janowiak, J., Rudolf, B., Schneider, U., Curtis, S., Bolvin, D., Gruber, A., Susskind, J., Arkin, P., and Nelkini, E.: The Version 2.1 Global Precipitation Climatology Project (GPCP) Monthly Precipitation Analysis (1979 -Present), J. Hydrometeor., 4(6), 1147-1167, https://doi.org/10.1175/1525-7541(2003)004<1147:TVGPCP>2.0.CO;2, 2003.

Ahn, M.-S., Kim, D., Kang, D., Lee, J., Sperber, K. R., and Glecker, P.

J., et al.: MJO propagation across the Maritime Continent: Are CMIP6 models better than CMIP5 models? Geophys. Res. Lett., 47, e2020GL087250, https://doi.org/10.1029/2020GL087250, 2020.

Ahn, M.-S., Kim, D., Sperber, K. R., Kang, I.-S., Maloney, E., Waliser, D., and Hendon, H.: MJO simulation in CMIP5 climate models: MJO skill metrics and process-oriented diagnosis, Clim. Dyn., 49, 4023–4045, https://doi.org/10.1007/s00382-017-3558-4, 2017.

Alappattu, D. P., Wang, Q., Kalogiros, J., Guy, N., and Jorgensen, D. P.: Variability of upper ocean thermohaline structure during a MJO event from DYNAMO aircraft observations, J. Geophys. Res. - Oceans, 122, 1122–1140, https://doi.org/10.1002/2016JC012137, 2017.

Amante, C., and Eakins, B. W.: ETOPO1 1 arc-minute globe relief model: Procedures, data sources and analysis, NOAA Tech. Memo. NESDIS NGDC-24, 19 pp., NOAA, Silver Spring, Md., 2009.

Behringer, D. W., and Xue, Y.: Evaluation of the global ocean data assimilation system at NCEP: The Pacific Ocean. Eighth Symposium on Integrated Observing and Assimilation Systems for Atmosphere, Oceans, and Land Surface, AMS 84th Annual Meeting, Washington State Convention and Trade Center, Seattle, Washington, 11-15. Derber, J.C., and A. Rosati, 1989: A global oceanic data assimilation system, J. Phys. Oceanogr., 19, 1333–1347, https://ams.confex.com/ams/pdfpapers/70720.pdf, 2004.

Bentsen, M., Bethke, I., Debernard, J. B., Iversen, T., Kirkevåg, A., Seland, Ø., Drange, H., Roelandt, C., Seierstad, I. A., Hoose, C., and Kristjánsson, J. E.: The Norwegian Earth System Model, NorESM1-M – Part 1: Description and basic evaluation of the physical climate, Geosci. Model Dev., 6, 687–720, https://doi.org/10.5194/gmd-6-687-2013, 2013.

Bernie, D., Guilyardi, E., Madec, G., Slingo, J., Woolnough, S., and Cole, J.: Impact of resolving the diurnal cycle in an ocean–atmosphere GCM. Part 2: a diurnally coupled CGCM, Clim. Dynam., 31, 909–925, https://doi.org/10.1007/s00382-008-0429-z, 2008.

Boyle, J. S., Klein, S. A., Lucas, D. D., Ma, H.-Y., Tannahill, J., and Xie, S.: The parametric sensitivity of CAM5's MJO, J. Geophys. Res.-Atmos., 120, 1424–1444, https://doi.org/10.1002/2014JD022507, 2015.

Bui, H. X., and Maloney, E. D.: Changes in Madden-Julian Oscillation precipitation and wind variance under global warming, Geophys. Res. Lett., 45, 7148–7155, https://doi.org/10.1029/2018GL078504, 2018.

Chang, M.-Y., Li, T., Lin, P.-L., and Chang, T.-H.: Forecasts of MJO

Events during DYNAMO with a Coupled Atmosphere-Ocean Model: Sensitivity to Cumulus Parameterization Scheme, J. Meteorol. Res., 33, 1016–1030, https://doi.org/10.1007/s13351-019-9062-5, 2019.

CLIVAR MADDEN–JULIAN OSCILLATION WORKING GROUP: MJO simulation diagnostics, J. Climate, 22, 3006–3030, https://doi.org/10.1175/2008JCLI2731.1, 2009.

Crueger, T., Stevens, B., and Brokopf, R.: The Madden–Julian Oscillation in ECHAM6 and the introduction of an objective MJO metric, J. Climate, 26, 3241–3257, https://doi.org/10.1175/JCLI-D-12-00413.1, 2013.

Danabasoglu, G., Lamarque, J.-F., Bacmeister, J., Bailey, D. A., DuVivier, A. K., and Edwards, J., et al.: The Community Earth System Model Version 2 (CESM2), J. Adv. Model. Earth Syst., 12, e2019MS001916, https://doi.org/10.1029/2019MS001916, 2020.

Dee, D. P., Uppala, S. M., Simmons, A. J., Berrisford, P., Poli, P., Kobayashi, S., Andrae, U., Balmaseda, M. A., Balsamo, G., Bauer, P., Bechtold, P., Beljaars, A. C. M., van de Berg, L., Bidlot, J., Bormann, N., Delsol, C., Dragani, R., Fuentes, M., Geer, A. J., Haimberger, L., Healy, S. B., Hersbach, H., Hólm, E. V., Isaksen, L., Kållberg, P., Köhler, M., Matricardi, M., McNally, A. P., Monge-Sanz, B. M., Morcrette, J.-J., Park, B.-K., Peubey, C., de Rosnay, P., Tavolato, C., Thépaut, J.-N., and Vitart, F.: The ERA-Interim reanalysis: configuration and performance of the data assimilation system, Q. J. R. Meteorol. Soc., 137: 553–597, https://doi.org/10.1002/qj.828, 2011.

de Szoeke, S. P., Skyllingstad, E. D., Zuidema, P., and Chandra, A. S.: Cold pools and their influence on the tropical marine boundary layer, J. Atmos. Sci., 74, 1149–1168. https://doi.org/10.1175/JAS-D-16-0264.1, 2017.

Delworth, T. L., et al.: GFDL's CM2 global coupled climate models. Part 1: Formulation and simulation characteristics, J. Climate, 19, 643–674, https://doi.org/10.1175/JCLI3629.1, 2006.

DeMott, C. A., Klingaman, N. P., and Woolnough, S. J.: Atmosphere-ocean coupled processes in the Madden-Julian oscillation, Rev. Geophys., 53, 1099–1154, https://doi.org/10.1002/2014RG000478, 2015.

DeMott, C. A., Klingaman, N. P., Tseng, W.-L., Burt, M. A., Gao, Y., and Randall, D. A.: The convection connection: How ocean feedbacks affect tropical mean moisture and MJO propagation, J. Geophys. Res.-Atmos., 124, 11,910–11,931, https://doi.org/10.1029/2019JD031015, 2019.

~~Gaspar, P., Gregoris, Y., and Lefevre, J.-M.: A simple eddy kinetic energy model for simulations of the oceanic vertical mixing: tests~~

~~at station papa and long-term upper ocean study site, J. Geophys. Res. -Oceans, 95, 16179–16193, https://doi.org/10.1029/JC095iC09p16179, 1990.~~

~~Gonzalez, A. O., and Jiang, X.: Winter mean lower tropospheric moisture over the Maritime Continent as a climate model diagnostic metric for the propagation of the Madden-Julian oscillation, Geophys. Res. Lett., 44, https://doi.org/10.1002/2016GL072430, 2017.~~

~~Grassl, H.: The dependence of the measured cool skin of the ocean on wind stress and total heat flux, Bounday-Layer Meteorol., 10, 465-474, https://doi.org/10.1007/BF00225865, 1976.~~

Haertel, P.: Prospects for Erratic and Intensifying Madden-Julian Oscillations, Climate, 8, 24, https://doi.org/10.3390/cli8020024, 2020.

Hannah, W. M., and Maloney, E. D.: The moist static energy budget in NCAR CAM5 hindcasts during DYNAMO, J. Adv. Model. Earth Syst., 6, 420–440, https://doi.org/10.1002/2013MS000272, 2014.

~~Hasse, L.: The sea surface temperature deviation and the heat flow at the sea–air interface, Bounday-Layer Meteorol., 1, 368-379, https://doi.org/10.1007/BF02186037, 1971.~~

Hagos, S. M., Zhang, C., Feng, Z., Burleyson, C. D., Mott, C. De, Kerns, B., Benedict, J. J., and Martini, M. N.: The impact of the diurnal cycle on the propagation of Madden-Julian Oscillation convection across the Maritime Continent, J. Adv. Model. Earth Syst., 8, 1552–1564, https://doi.org/10.1002/2016MS000725, 2016.

He, S., Yang, S., and Li, Z.: Influence of Latent Heating over the Asian and Western Pacific Monsoon Region on Sahel Summer Rainfall, Sci. Rep. 7, 7680, https://doi.org/10.1038/s41598-017-07971-6, 2017.

Heath, A., Gonzalez, A. O., Gehne, M., and Jaramillo, A.: Interactions of large-scale dynamics and Madden-Julian Oscillation propagation in multi-model simulations, J. Geophys. Res.-Atmos., 126, e2020JD033988. https://doi.org/10.1029/2020JD033988, 2021.

Hong, X., Reynolds, C. A., Doyle, J. D., May, P., and O'Neill, L.: Assessment of upper-ocean variability and the Madden-Julian Oscillation in extended-range air–ocean coupled mesoscale simulations, Dyn. Atmos. Oceans, 78, 89–105. https://doi.org/10.1016/j.dynatmoce.2017.03.002, 2017.

Hung, M.-P., Lin, J.-L., Wang, W., Kim, D., Shinoda, T., and Weaver, S. J.: MJO and convectively coupled equatorial waves simulated by CMIP5 climate models, J. Climate, 26, 6185–6214, https://doi.org/10.1175/JCLI-D-12-00541.1, 2013.

Hurrell, J. W., Holland, M. M., Gent, P. R., Ghan, S., Kay, J. E., Kushner, P. J., Lamarque, J.-F., Large, W. G., Lawrence, D., Lindsay, K., Lipscomb, W. H., Long, M. C., Mahowald, N., Marsh, D. R., Neale, R. B., Rasch, P., Vavrus, S., Vertenstein, M., Bader, D., Collins, W. D., Hack, J. J., Kiehl, J., and Marshall, S.: The community Earth system model: A framework for collaborative research, B. Am. Meteorol. Soc., 94, 1319–1360, https://doi.org/10.1175/BAMS-D-12-00121, 2013.

Jiang, X., et al.: Vertical structure and physical processes of the MaddenJulian oscillation: Exploring key model physics in climate simulations, J. Geophys. Res.-Atmos., 120, 4718–4748, https://doi.org/10.1002/2014JD022375, 2015.

Jiang, X., Adames, Á. F., Kim, D., Maloney, E. D., Lin, H., and Kim, H., et al.: Fifty years of research on the Madden-Julian Oscillation: Recent progress, challenges, and perspectives, J. Geophys. Res.-Atmos., 125, e2019JD030911, https://doi.org/10.1029/2019JD030911, 2020.

Johnson, R. H., and Ciesielski, P. E.: Multiscale variability of the atmospheric boundary layer during DYNAMO, J. Atmos. Sci., 74, 4003–4021, https://doi.org/10.1175/JAS-D-17-0182.1, 2017.

Kaylor, R. E.: Filtering and decimation of digital time series, Tech. Rep. Note BN 850, Institute for Physical Science and Technology, University of Maryland at College Park, 14 pp~~, 1997~~., 1977.

Kim, D., Sobel, A. H., Maloney, E. D., Frierson, D. M~~.~~., and Kang, I.-S.: A systematic relationship between intraseasonal variability and mean state bias in AGCM simulations, J. Climate, 24, 5506–5520. https://doi.org/10.1175/2011JCLI4177.1, 2011.

Kim, D., Kim H., and Lee, M.-I.: Why does the MJO detour the Maritime Continent during austral summer? Geophys. Res. Lett., 44, 2579–2587, https://doi.org/10.1002/2017GL072643, 2017.

Kim, H.-M., Hoyos, C. D~~.~~., and Webster, P. J. et al.: Ocean–atmosphere coupling and the boreal winter MJO, Clim Dynam., 35, 771–784, https://doi.org/10.1007/s00382-009-0612-x, 2010.

Kiranmayi, L., and Maloney, E. D.: Intraseasonal moist static energy budget in reanalysis data, J. Geophys. Res., 116, D21117, https://doi.org/10.1029/2011JD016031, 2011.

Lan, Y.-Y., Tsuang, B.-J., Tu, C.-Y., Wu, T.-Y., Chen, Y.-L., and Hsieh, C.-I.: Observation and Simulation of Meteorology and Surface Energy Components over the South China Sea in Summers of 2004 and 2006, Terr. Atmos. Ocean. Sci., 21, 325~~–~~–342, https://doi.org/ 10.3319/TAO.2009.04.07.01(A), 2010.

Lee, H.-T., and NOAA CDR Program: NOAA Climate Data Record (CDR) of Daily Outgoing Longwave Radiation (OLR), Version 1.2, NOAA National Climatic Data Center, https://doi.org/10.7289/V5SJ1HH2, 2011.

Li, T., Ling, J., and Hsu, P.-C.: Madden–Julian Oscillation: Its discovery, dynamics, and impact on East Asia, J. Meteor. Res., 34, 20–42, https://doi.org/10.1007/s13351-020-9153-3, 2020.

Li, T., Tam, F., Fu, X., Zhou, T., and Zhu, W.: Causes of the intraseasonal SST variability in the tropical Indian Ocean, Atmos. Oceanic Sci. Lett., 1, 18–23, https://doi.org/10.1080/16742834.2008.11446758, 2008.

Li, X., Tang, Y., Zhou, L., Chen, D.~~-~~., and Yao, Z.: Assessment of Madden–Julian oscillation simulations with various configurations of CESM, Clim. Dynam., 47, 2667–2690, https://doi.org/10.1007/s00382-016-2991-0, 2016.

Ling, J., Zhao, Y.~~-~~., and Chen, G.: Barrier effect on MJO propagation by the Maritime Continent in the MJO Task Force/GEWEX atmospheric system study models, J. Climate, 32, 5529–5547, https://doi.org/10.1175/JCLI-D-18-0870.1, 2019.

Madden, R. A., and Julian, P. R.: Description of global-scale circulation cells in the tropics with a 40-50 day period, J. Atmos. Sci., 29, 1109-1123, https://doi.org/10.1175/1520-0469(1972)029<1109:DOGSCC>2.0.CO;2, 1972.

Madden, R. A., and Julian, P. R.: Observations of the 40-50 day tropical oscillation - A review, Mon. Weather Rev., 122, 814– 837, https://doi.org/10.1175/1520-0493(1994)122<0814:OOTDTO>2.0.CO;2, 1994.

~~Mellor, G. L., and Yamada, T.: Development of a turbulence closure model for geophysical fluid problems, Rev. Geophys., 20, 851-875, https://doi.org/10.1029/RG020i004p00851, 1982.~~

Neale, R. B., et al.,: Description of the NCAR Community Atmosphere Model (CAM 5.0), NCAR Tech. Note NCAR/TN-486+STR, 289 pp., Natl. Cent. for Atmos. Res, Boulder, Colo., 2012.

Newman, M., Sardeshmukh, P. D., and Penland, C.: How important is air–sea coupling in ENSO and MJO evolution? J. Clim., 22, 2958– 2977, https://doi.org/10.1175/2008JCLI2659.1, 2009.

Oh, J., Kim, B., and Kim, K. et al.: The impact of the diurnal cycle on the MJO over the Maritime Continent: a modeling study assimilating TRMM rain rate into global analysis, Clim. Dynam., 40, 893–911, https://doi.org/10.1007/s00382-012-1419-8, 2013.

~~Paulson, C. A. and Simpson, J. J.: The temperature difference across the cool skin of the ocean, J. Geophys. Res., 86, 11044-11054, https://doi.org/10.1029/JC086iC11p11044, 1981.~~

Pei, S., Shinoda, T., Soloviev, A., and Lien, R.-C.: Upper ocean response to the atmospheric cold pools associated with the Madden-Julian Oscillation, Geophys. Res. Lett., 45, 5020–5029, https://doi.org/10.1029/2018GL077825, 2018.

Pujiana, K., Moum, J. N., and Smyth, W. D.: The role of subsurface turbulence in redistributing upper-ocean heat, freshwater, and momentum in response to the MJO in the equatorial Indian Ocean, J. Phys. Oceanogr., 48, 197–220, https://doi.org/10.1175/JPO-D-17-0146.1, 2018.

Rayner, N. A., Parker, D. E., Horton, E. B., Folland, C. K., Alexander, L. V., Rowell, D. P., Kent, E. C., and Kaplan, A.: Global analyses of sea surface temperature, sea ice, and night marine air temperature since the late nineteenth century, J. Geophys. Res., 108(D14), 4407, https://doi.org/10.1029/2002JD002670, 2003.

Ren, P. F., Gao, L., and Ren, H.-L. et al.: Representation of the Madden–Julian Oscillation in CAMSCSM, J. Meteor. Res., 33, 627–650, https://doi.org/10.1007/s13351-019-8118-x, 2019.

Reynolds, R. W., and Smith, T. M.: A high-resolution global sea surface temperature climatology, J. Clim., 8(6),1571–1583, https://doi.org/10.1175/1520-0442(1995)008<1571:AHRGSS>2.0.CO;2, 1995.

Schreck, C. J., Lee, H.-T., and Knapp, K. R.: HIRS outgoing longwave radiation—Daily climate data record: Application toward identifying tropical subseasonal variability, Remote Sens., 10, 1325. https://doi.org/10.3390/rs10091325, 2018.

Sobel, A. H., Maloney, E. D., Bellon, G., and Dargan, M. F.: The role of surface heat fluxes in tropical intraseasonal oscillations, Nat. Geosci., 1, 653–657, https://doi.org/10.1038/ngeo312, 2008.

Subramanian, A. C., Jochum, M., Miller, A. J., Murtugudde, R., Neale, R. B., and Waliser, D. E.: The Madden–Julian oscillation in CCSM4, J. Climate, 24, 6261–6282, https://doi.org/10.1175/JCLI-D-11-00031.1, 2011.

Tseng, W.-L., Tsuang, B.-J., Keenlyside, N. S., Hsu, H.-H. and Tu, C.-Y.: Resolving the upper-ocean warm layer improves the simulation of the Madden-Julian oscillation, Clim. Dynam., 44, 1487–1503, https://doi.org/10.1007/s00382-014-2315-1, 2014.

Tseng, W.-L., Hsu, H.-H., Keenlyside, N., Chang, C.-W. J., Tsuang, B.-J., Tu, C.-Y., and Jiang, L.-C.: Effects of Orography and Land–Sea Contrast on the Madden–Julian Oscillation in the Maritime Continent: A Numerical Study Using ECHAM-SIT, J. Climate, 30, 9725–9741, https://doi.org/10.1175/JCLI-D-17-0051.1, 2017.

Tu, C.-Y., and Tsuang, B.-J.: Cool-skin simulation by a one-column ocean model, Geophys. Res. Lett., 32, L22602, https://doi.org/10.1029/2005GL024252, 2005.

Wang, W., Saha, S., Pan, H.-L., Nadiga, S., and White, G.: Simulation of ENSO in the new NCEP Coupled Forecast System Model (CFS03), Mon. Wea. Rev., 133, 1574–1593, https://doi.org/10.1175/MWR2936.1, 2005.

Wang, W., Hung, M.-P., Weaver, S. J., Kumar, A., and Fu, X.: MJO prediction in the NCEP Climate Forecast System version 2, Clim. Dyn., 42, 2509–2520, https://doi.org/10.1007/s00382-013-1806-9, 2014.

Wheeler, M. C~~,~~., and Hendon, H. H.: An all-season real-time multivariate MJO index: development of an index for monitoring and prediction, Mon. Weather Rev., 132, 1917–1932, https://doi.org/10.1175/1520-0493(2004)132<1917:AARMMI>2.0.CO;2, 2004.

Wheeler, M., and Kiladis, G. N.: Convectively coupled equatorial waves: Analysis of clouds and temperature in the wavenumber-frequency domain, J. Atmos. Sci., 56, 374– 399, https://doi.org/10.1175/1520-0469(1999)056<0374:CCEWAO>2.0.CO;2, 1999.

Woolnough, S. J., Vitard, F., and Balmaseda, M. A.: The role of the ocean in the Madden–Julian oscillation: Implications for MJO prediction, Quart. J. Roy. Meteor. Soc., 133, 117–128, https://doi.org/10.1002/qj.4, 2007.

Wu, ~~J.: On the cool skin of the ocean, Bounday-Layer Meteorol., 31, 203-207, https://doi.org/10.1007/BF00121179, 1985.~~

~~Wu,~~ C.-H., and Hsu, H.-H.: Potential Influence of Topography on the MJO in the Maritime Continent, J. Climate, 22, 5433~~–~~–5448, https://doi.org/10.1175/2009JCLI2825.1, 2009.

Yoneyama, K., Zhang, C., and Long, C.: Tracking pulses of the Madden–Julian oscillation, Bull. Amer. Meteor. Soc., 94, 1871–1891, https://doi.org/10.1175/BAMS-D-12-00157.1, 2013.

Zhang, C.: Madden-Julian oscillation, Rev. Geophys., 43, RG2003, https://doi.org/10.1029/2004RG000158, 2005.

Zhang, C., and Yoneyama, K.: CINDY/DYNAMO field campaign: Advancing our understanding of MJO initiation~~. The Global Monsoon System, C.-P. Chang et al., Eds.,~~., In World Scientific Series on Asia-Pacific Weather and Climate~~,~~ (pp. 339-348). (World Scientific Series on Asia-Pacific Weather and Climate; Vol. Volume 9~~,~~), World Scientific Publishing Co~~., 339–348,~~. Pte Ltd. https://doi.org/10.1142/9789813200913_0027, 2017.

Table 1. List of experiments

Section	Category	Experiments	Description
~~4~~3.1	Coupled or uncoupled	A–CTL	Standalone CAM5.3 forced by ~~observed~~forced by the monthly mean Hadley Centre SST dataset version 1 climatology
		C–30NS (the control coupled experiment)	CAM5.3 coupled with SIT over the tropical domain (30°~~S~~N–30°~~N~~S), with 41 layers of finest vertical resolution (up to ~~submarine topography~~the seabed) and diurnal cycle; the frequency of CAM5 being exchanged with CPL is 48 times per day
~~4~~3.2	Upper-ocean vertical resolution	C–LR12m	The first ocean vertical level starts at 11.~~8~~5 m with 31 layers (beside SST and cool skin layer are 11.5 m, 29.5 m and 43.6 m up to the seabed)
		C–LR34m	The first ocean vertical level starts at ~~34.2 m~~33.9 m with 28 layers (beside SST and cool skin layer are 33.9 m, 76.9 m and 96.8 m up to the seabed)
~~4~~3.3	Lowest boundary of SIT	C–HR1mB10m	The lowest boundary of SIT has a depth of 10 m (~~middle grid~~model depth between 0 m and 10 m)
		C–HR1mB30m	The lowest boundary of SIT has a depth of 30 m (~~middle grid~~model depth between 0 m and 30 m)
		C–HR1mB60m	The lowest boundary of SIT has a depth of 60 m (~~middle grid~~model depth between 0 m and 60 m)
~~4~~3.4	Regional coupling domain in latitude	C–0_30N	Coupled in the tropical northern hemisphere (0°N–30°N, 0°E–360°E)
		C–0_30S	Coupled in the tropical southern hemisphere (0°S–30°S, 0°E–360°E)
	Regional coupling domain in longitude	C–30_180E	Coupled in the Indo-Pacific (30°~~S~~N–30°~~N~~S, 30°E–180°E)
		C–30E_75W	Coupled over the Indian Ocean and Pacific Ocean (30°~~S~~N–30°~~N~~S, 30°E–75°W)
~~4~~3.5	Absence of the diurnal cycle	C–30NS–nD	Absence of the diurnal cycle in C–30NS; the CAM5.3 daily atmospheric mean of surface wind, temperature, total precipitation, net surface heat flux, u-stress and v-stress over water trigger the SIT and daily mean SST feedback to atmosphere; the frequency of CAM5 is exchanged with CPL 48 times per day

~~The CAM5.3 AGCM is used in all experiments~~

Experiment abbreviations: “A” means standalone AGCM simulation. “C” means the CAM5.3 coupled to the SIT model.

Figure List

Figure 1. Schematics of coupled and uncoupled domains in the regional coupling experiment: (a) C–30NS, (b) C–0_30N, (c) C–0_30S, (d) C–30_180E, and (e) C–30E_75W. The background is the climatological mean SST in December–February (DJF).

Figure 2. (a)–(c) Zonal wavenumber–frequency spectra for 850-hPa zonal wind averaged over 10°S–10°N in boreal winter after removing the climatological mean seasonal cycle. Vertical dashed lines represent periods at 80 and 30 days, respectively. (d)–(f) Hovmöller diagrams of the correlation between the precipitation averaged over 10°S–5°N, 75–100°E and the intraseasonally filtered precipitation (color) and 850-hPa zonal wind (contour) averaged over 10°N–10°S. (g)–(i) Zonal wavenumber–frequency power spectra of anomalous OLR (colors) and phase lag with U850 (vectors) for the symmetric component of tropical waves, with the vertically upward vector representing a phase lag of 0° with phase lag increasing clockwise. Three dispersion straight lines with increasing slopes represent the equatorial Kelvin waves (derived from the shallow water equations) corresponding to three equivalent depths, 12, 25, and 50 m, respectively. (j)–(l) Composites of 20–100-day filtered OLR (W m^{-2}, shaded) and 850-hPa wind (m s^{-1}, vector) for MJO phase 5 when deep convection is the strongest over the MC and 850-hPa wind, with the reference vector (1 m s^{-1}) shown at the top right of each panel, and (m)–(o) 15°N–15°S averaged p-vertical velocity anomaly (Pa s^{-1}, shaded) and moist static energy anomaly (W m^{-2}, contour, interval 0.003); solid, dashed, and thick-black lines represent positive, negative, and zero values, respectively. The number of days used to generate the composite is shown at the bottom right corner of each panel. (a), (d), (g), (j), and (m) are from ~~observations;~~the ERA-Interim and NOAA post-processed data (abbr. ERA-I/NOAA); (b), (e), (h), (k), and (n) are from the control experiment C–30NS; and (c), (f), (i), (l), and (o) are from the A–CTL.

Figure 3. Evolution of the filtered OLR anomaly (W m^{-2}, shaded) and 850-hPa wind (m s^{-1}, vector) at phase 2, 4, 6, and 8: (a) ~~observation~~the ERA-I/NOAA data, (b) the control coupled experiment C–30NS, and (c) the uncoupled experiment A–CTL. The unit of the reference vector shown at the top right corner of each panel is m s^{-1}, and the number of days used for the composite is shown at the bottom right corner of each panel.

Figure 4. (a)–(c) Phase-longitude Hovmöller diagrams of 20–100-day filtered precipitation (mm day^{-1}, shaded) and SST anomaly (K, contour) averaged over 10°N–10°S from phase 1 to 8. Contour interval is 0.03; solid, dashed, and thick-black lines represent positive, negative, and zero values, respectively. (d)–(f) Phase-vertical Hovmöller diagrams of 20–100-day moisture divergence (shading, 10^{-6} g kg^{-1} s^{-1}) and

zonal wind (contoured, m s^{-1}) averaged over 10°N–10°S, 120–150°E; solid, dashed, and thick-black curves are positive, negative, and zero values, respectively. (g)–(i) Variation of 30–60-day filtered precipitation in the eastern IO and the WP in observation (color shading), and the ratio between intraseasonal and total variance (contoured) and (j)–(l) composites 20–100-day filtered SST (K, shaded) and 850-hPa winds (m s^{-1}, vector) at phase 7 when deep convection was the strongest over the dateline. Reference vector shown at the top right corner of each panel. (a), (d), (g), and (j) are from the ~~observation~~ERA-I/NOAA data; (b), (e), (h), and (k) are from the control coupled experiment C–30NS; and (c), (f), (i), and (l) are from the uncoupled experiment A–CTL.

Figure 5. (a)–(b) Same as in Fig. 2(a) but for the C~~–~~_LR12m and C~~–~~_LR34m. (c)–(d) Same as in Fig. 2(d) but for the C~~–~~_LR12m and C~~–~~_LR34m. (e)–(f) Same as in Fig. 4(a) but for the C~~–~~_LR12m and C~~–~~_LR34m.

Figure 6. Same as in Fig. 5 but for the C–HR1mB10m, C–HR1mB30m, and C–HR1mB60m.

Figure 7. Same as in Fig. 5 but for the C–0_30N, C–0_30S, C–30_180E, and C–30E_75W.

Figure 8. Same as in Fig. 3 but for phase 5 in the C–0_30N, C–0_30S, C–30_180E, and C–30E_75W.

Figure 9. Similar as in Fig. 5 but for the C–30NS–nD.

Figure 10. Scattered plots of various MJO indices in ~~observation~~the ERA-I/NOAA data and 12 experiments: (a) power ratio of east/west propagating waves of wavenumber 1–3 of 850-hPa zonal winds (X-axis) with a 30–80-day period and eastward propagation speed of U850 anomaly (Y-axis) from the Hovmöller diagram and (b) RMM1 and RMM2 variance and eastward propagation speed of the filtered precipitation anomaly derived from the Hovmöller diagram.

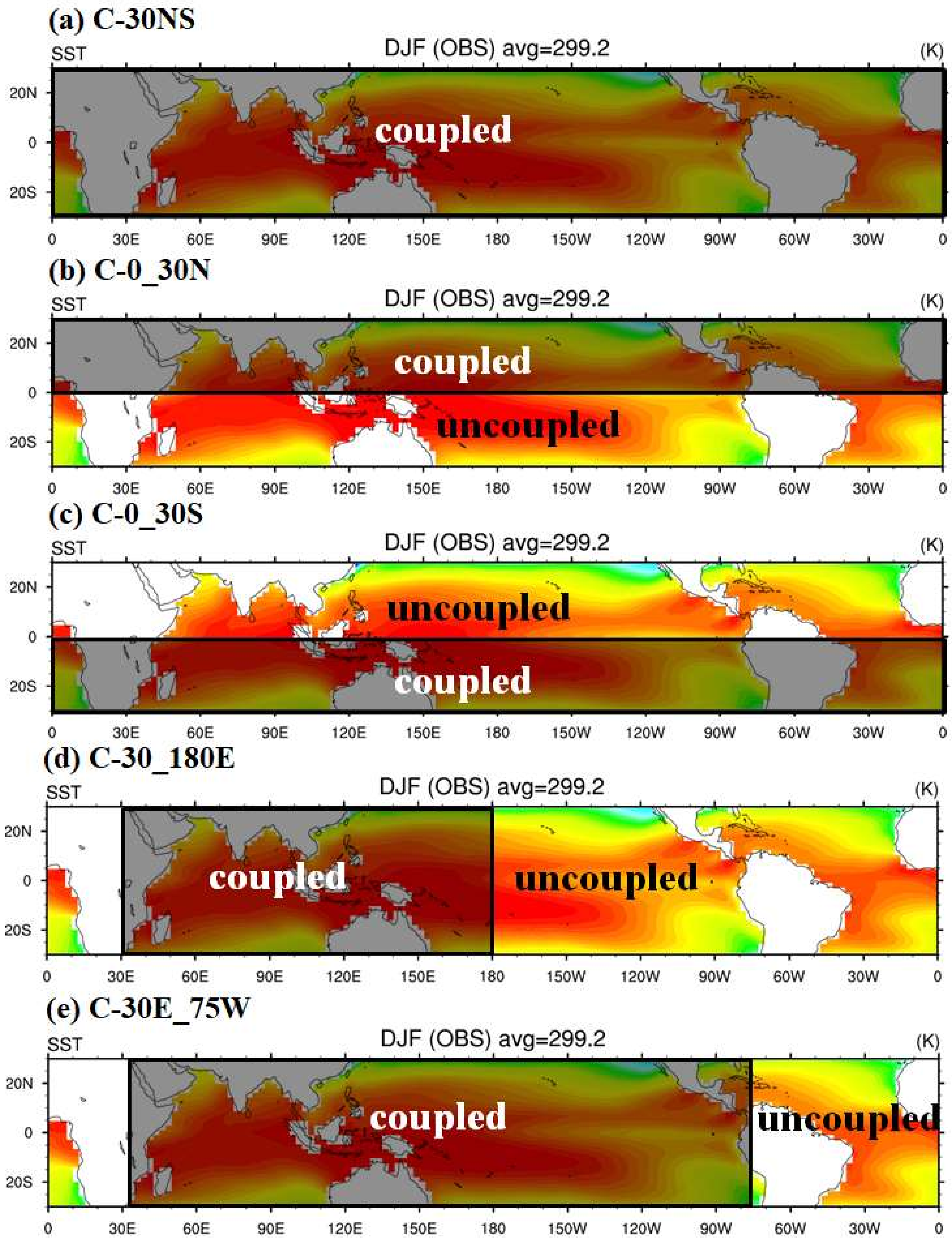

(a) C-30NS
SST
DJF (OBS) avg=299.2
(K)
coupled
(b) C-0_30N
SST
DJF (OBS) avg=299.2
(K)
coupled
uncoupled
(c) C-0_30S
SST
DJF (OBS) avg=299.2
(K)
uncoupled
coupled
(d) C-30_180E
SST
DJF (OBS) avg=299.2
(K)
coupled
uncoupled
(e) C-30E_75W
SST
DJF (OBS) avg=299.2
(K)
coupled
uncoupled
20N
0
20S
0
30E
60E
90E
120E
150E
180
150W
120W
90W
60W
30W
0

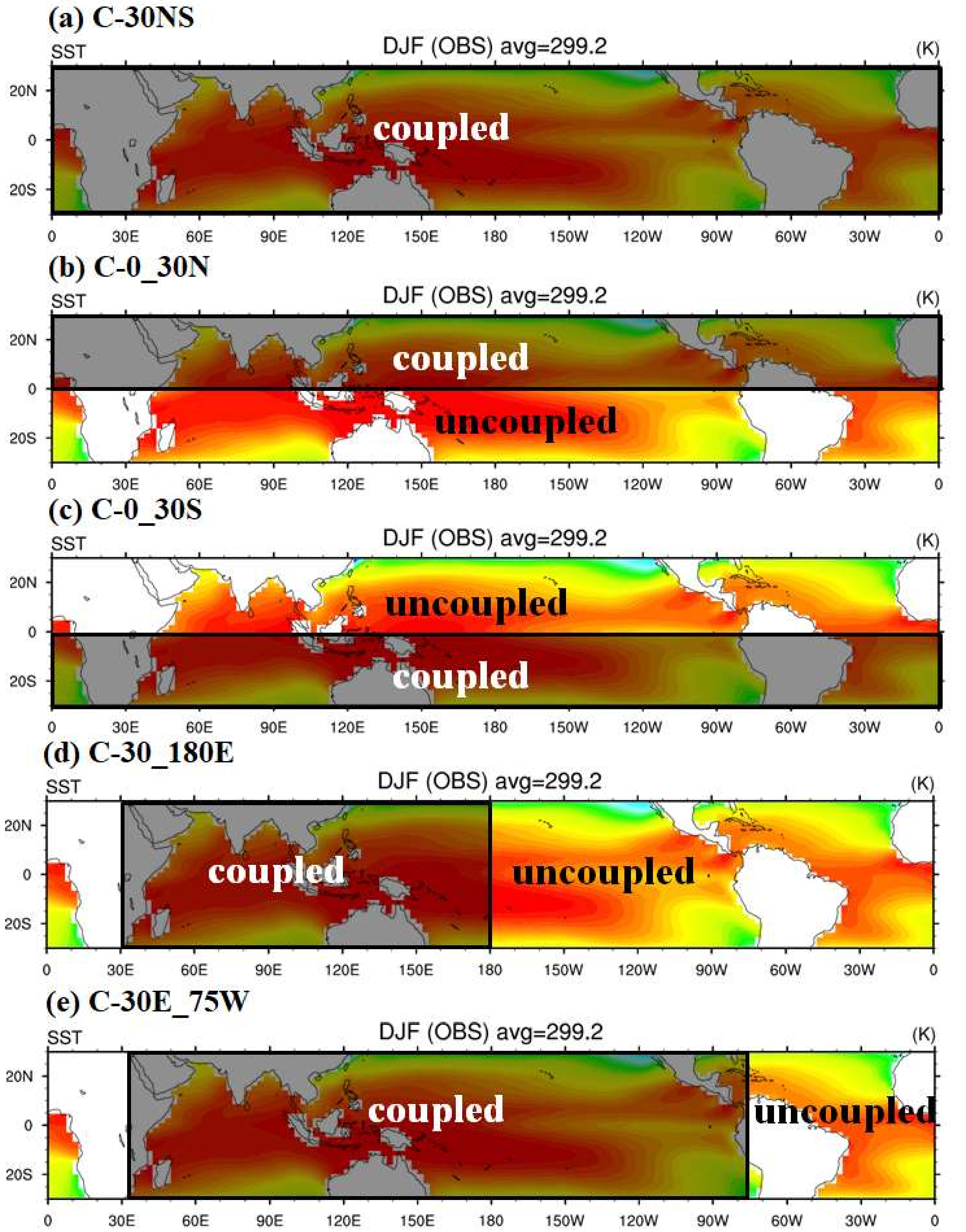

Figure 1. Schematics of coupled and uncoupled domains in the regional coupling experiment: (a) C–30NS, (b) C–0_30N, (c) C–0_30S, (d) C–30_180E, and (e) C–30E_75W. The background is the climatological mean SST in December–February (DJF).

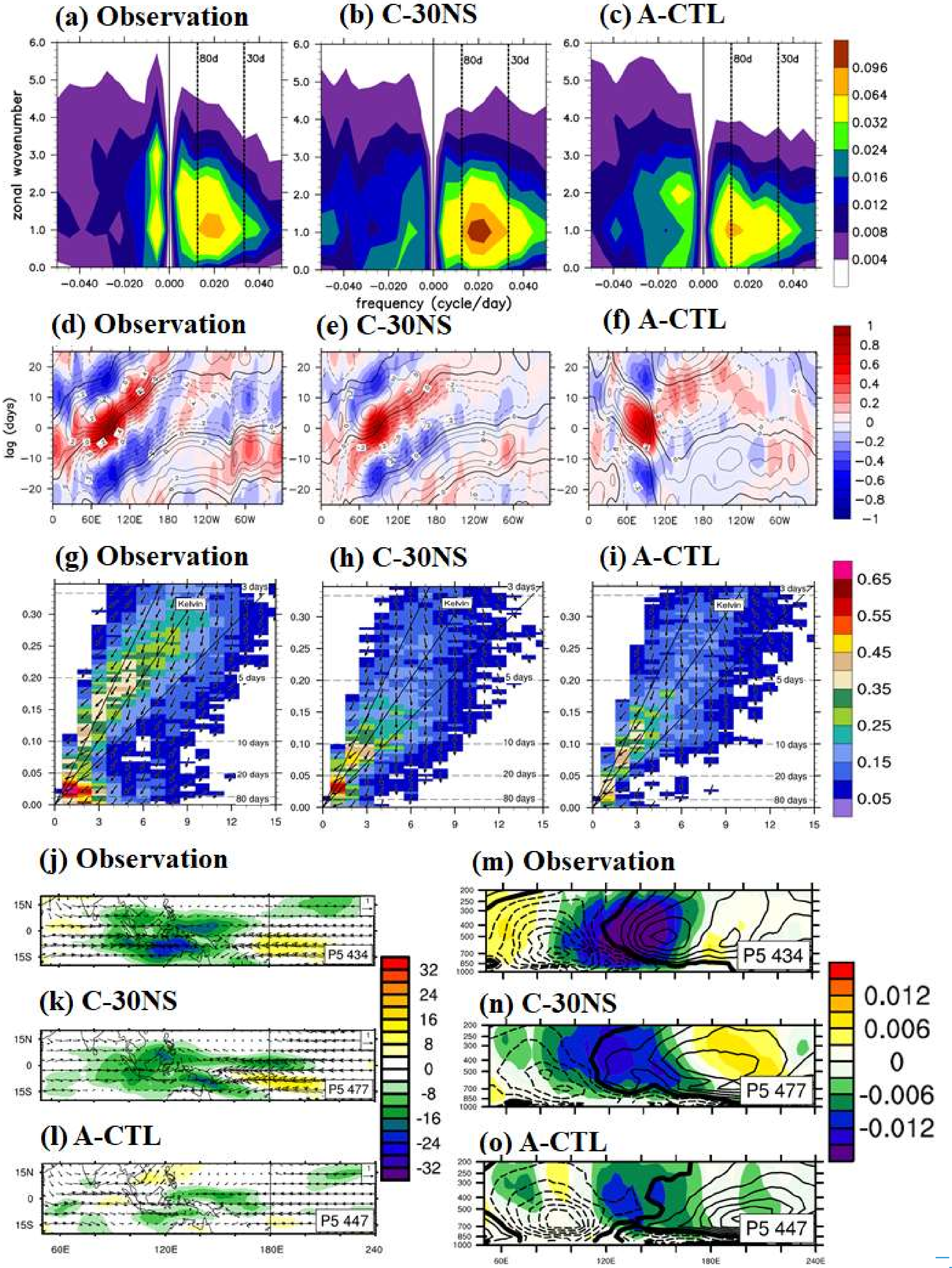
(a) Observation
(b) C-30NS
(c) A-CTL
zonal wavenumber
frequency (cycle/day)
80d
30d
0.096
0.064
0.032
0.024
0.016
0.012
0.008
0.004
(d) Observation
(e) C-30NS
(f) A-CTL
lag (days)
0
60E
120E
180
120W
60W
(g) Observation
(h) C-30NS
(i) A-CTL
Kelvin
3 days
5 days
10 days
20 days
80 days
0.65
0.55
0.45
0.35
0.25
0.15
0.05
(j) Observation
(k) C-30NS
(l) A-CTL
P5 434
P5 477
P5 447
32
24
16
8
0
-8
-16
-24
-32
(m) Observation
(n) C-30NS
(o) A-CTL
0.012
0.006
0
-0.006
-0.012

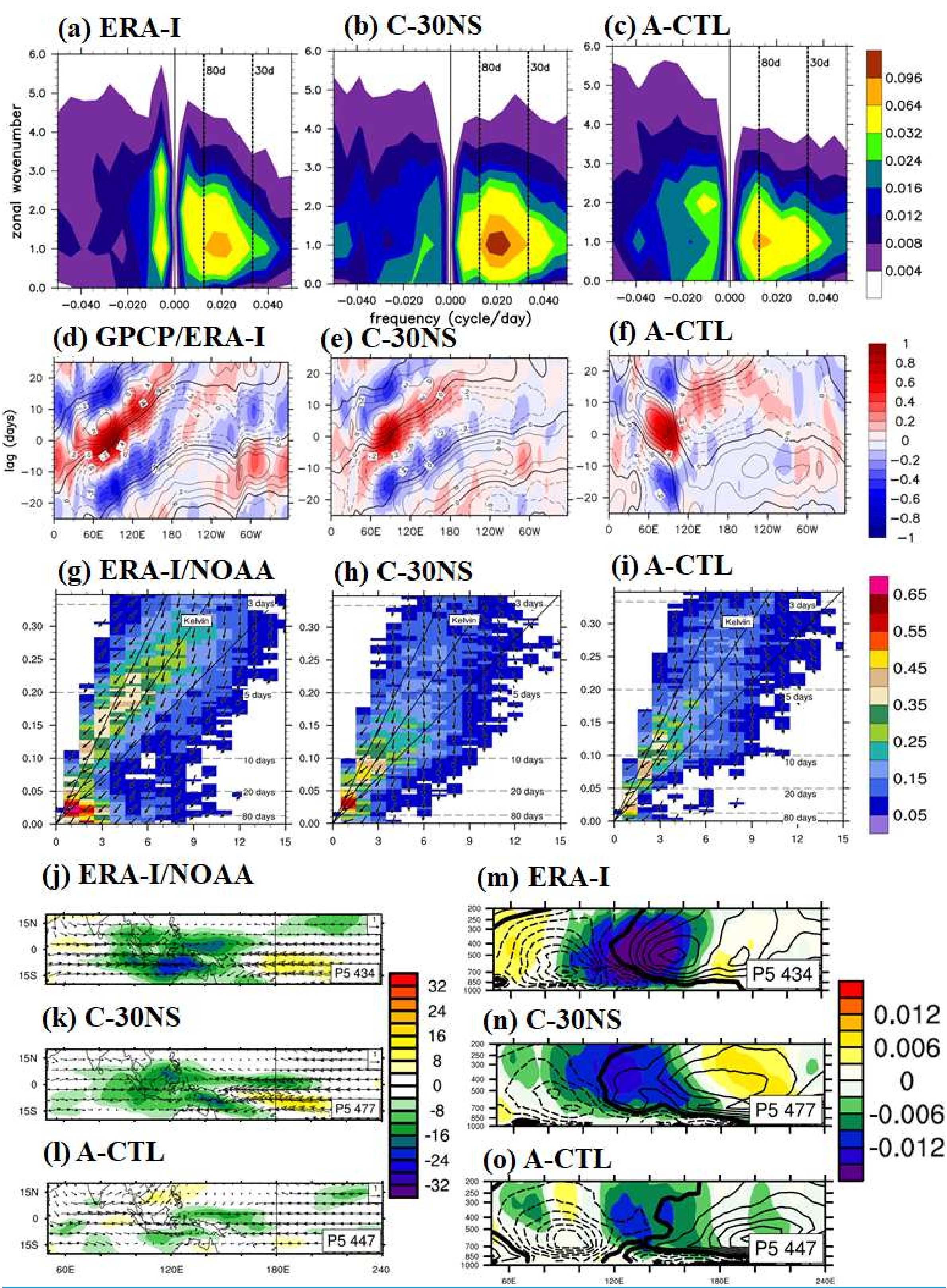

Figure 2. (a)–(c) Zonal wavenumber–frequency spectra for 850-hPa zonal wind averaged over 10°S–10°N in boreal winter after removing the climatological mean seasonal cycle. Vertical dashed lines represent periods at 80 and 30 days, respectively. (d)–(f) Hovmöller

diagrams of the correlation between the precipitation averaged over 10°S–5°N, 75–100°E and the intraseasonally filtered precipitation (color) and 850-hPa zonal wind (contour) averaged over 10°N–10°S. (g)–(i) Zonal wavenumber–frequency power spectra of anomalous OLR (colors) and phase lag with U850 (vectors) for the symmetric component of tropical waves, with the vertically upward vector representing a phase lag of 0° with phase lag increasing clockwise. Three dispersion straight lines with increasing slopes represent the equatorial Kelvin waves (derived from the shallow water equations) corresponding to three equivalent depths, 12, 25, and 50 m, respectively. (j)–(l) Composites of 20–100-day filtered OLR (W m^{-2}, shaded) and 850-hPa wind (m s^{-1}, vector) for MJO phase 5 when deep convection is the strongest over the MC and 850 hPa wind, with the reference vector (1 m s^{-1}) shown at the top right of each panel, and (m)–(o) 15°N–15°S averaged p-vertical velocity anomaly (Pa s^{-1}, shaded) and moist static energy anomaly (W m^{-2}, contour, interval 0.003); solid, dashed, and thick-black lines represent positive, negative, and zero values, respectively. The number of days used to generate the composite is shown at the bottom right corner of each panel. (a), (d), (g), (j), and (m) are from ~~observations;~~the ERA-Interim and NOAA post-processed data (abbr. ERA-I/NOAA); (b), (e), (h), (k), and (n) are from the control experiment C–30NS; and (c), (f), (i), (l), and (o) are from the A–CTL.

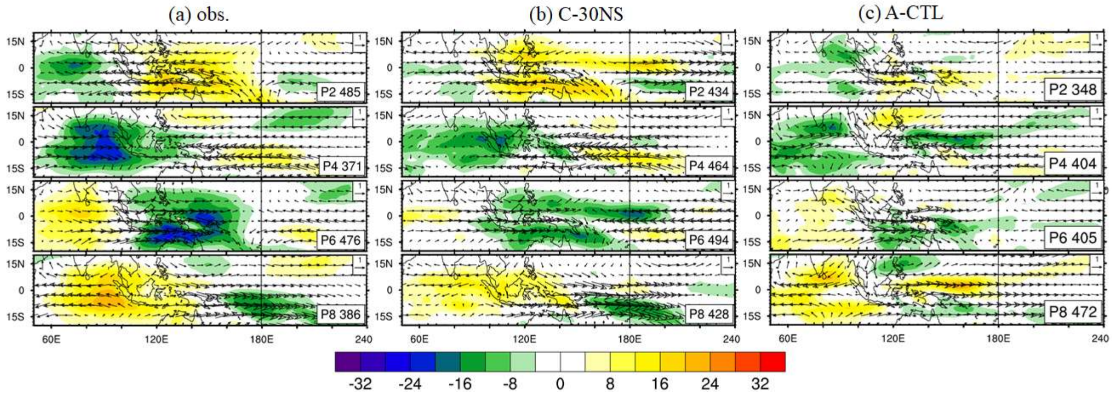

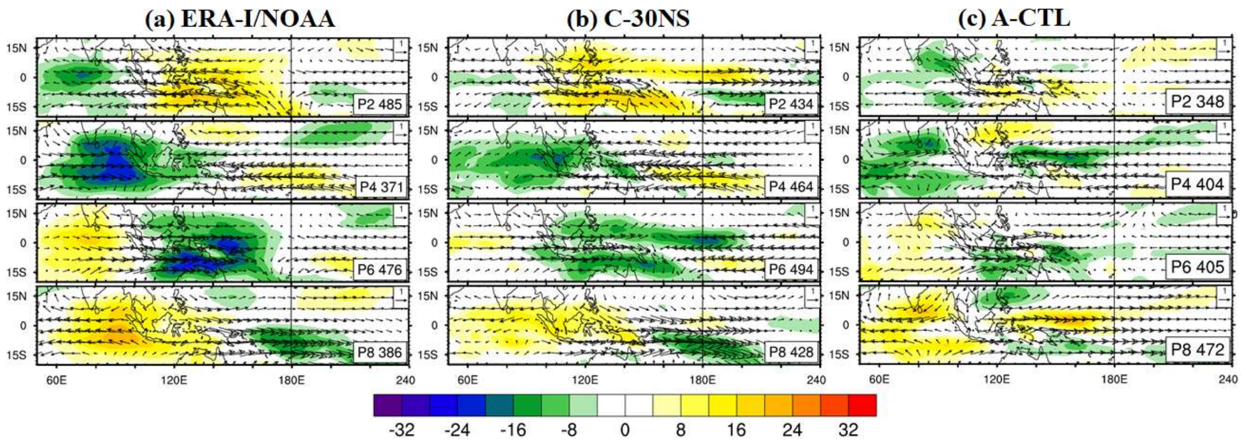

Figure 3. Evolution of the filtered OLR anomaly (W m^{-2}, shaded) and 850-hPa wind (m s^{-1}, vector) at phase 2, 4, 6, and 8: (a) ~~observation~~the ERA-I/NOAA data, (b) the control coupled experiment C–30NS, and (c) the uncoupled experiment A–CTL. The unit of the reference vector shown at the top right corner of each panel is m s^{-1}, and the number of days used for the composite is shown at the bottom right corner of each panel.

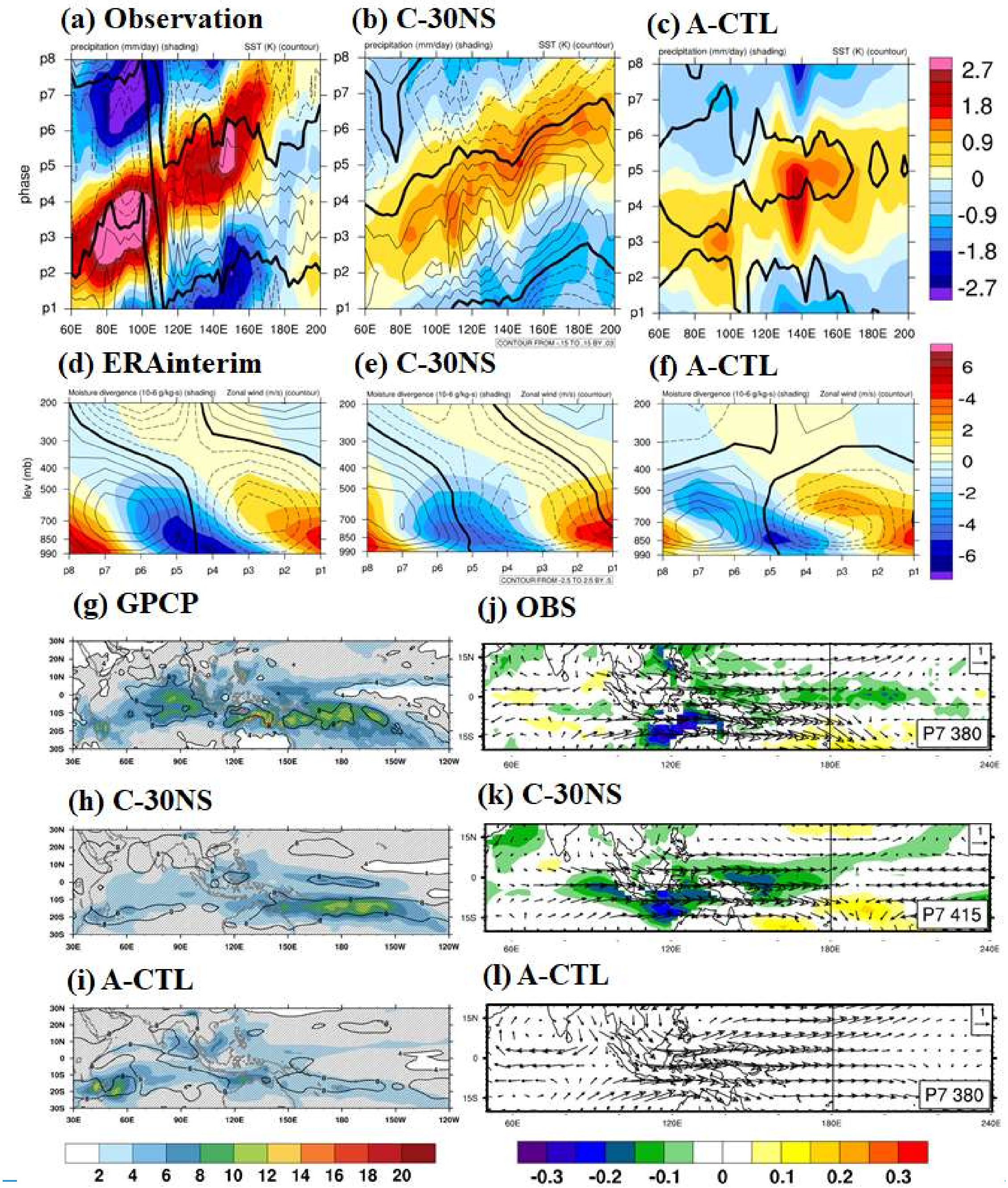
(a) Observation
(b) C-30NS
(c) A-CTL
precipitation (mm/day) (shading)
SST (K) (countour)
phase
p1 p2 p3 p4 p5 p6 p7 p8
60E 80E 100E 120E 140E 160E 180E 200
2.7 1.8 0.9 0 -0.9 -1.8 -2.7
(d) ERAinterim
(e) C-30NS
(f) A-CTL
lev (mb)
200 300 400 500 700 850 990
6 4 2 0 -2 -4 -6
(g) GPCP
(h) C-30NS
(i) A-CTL
30E 60E 90E 120E 150E 180 150W 120W
2 4 6 8 10 12 14 16 18 20
(j) OBS
(k) C-30NS
(l) A-CTL
P7 380
P7 415
P7 380
60E 120E 180E 240E
-0.3 -0.2 -0.1 0 0.1 0.2 0.3

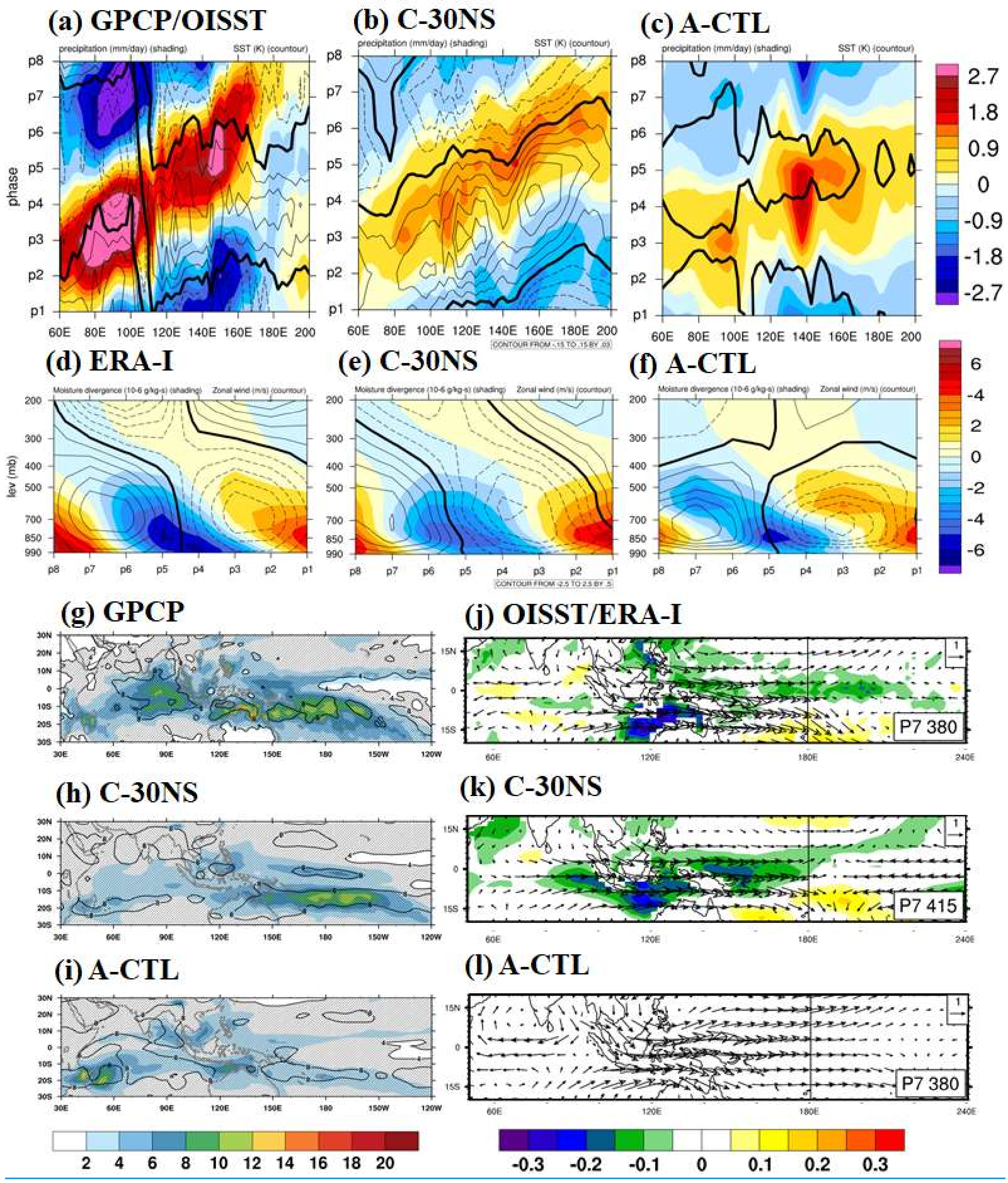

Figure 4. (a)–(c) Phase-longitude Hovmöller diagrams of 20–100-day filtered precipitation (mm day^{-1}, shaded) and SST anomaly (K, contour) averaged over 10°N–10°S from phase 1 to 8. Contour interval is 0.03; solid, dashed, and thick-black lines represent positive, negative, and zero values, respectively. (d)–(f) Phase-vertical Hovmöller diagrams of 20–100-day moisture divergence (shading, 10^{-6} g kg^{-1} s^{-1}) and zonal wind (contoured, m s^{-1}) averaged over 10°N–10°S, 120–150°E; solid, dashed, and thick-black curves are positive, negative, and zero values, respectively. (g)–(i) Variation

of 30–60-day filtered precipitation in the eastern IO and the WP in observation (color shading), and the ratio between intraseasonal and total variance (contoured) and (j)–(l) composites 20–100-day filtered SST (K, shaded) and 850-hPa winds (m s^{-1}, vector) at phase 7 when deep convection was the strongest over the dateline. Reference vector shown at the top right corner of each panel. (a), (d), (g), and (j) are from the ~~observation~~ERA-I/NOAA data; (b), (e), (h), and (k) are from the control coupled experiment C–30NS; and (c), (f), (i), and (l) are from the uncoupled experiment A–CTL.

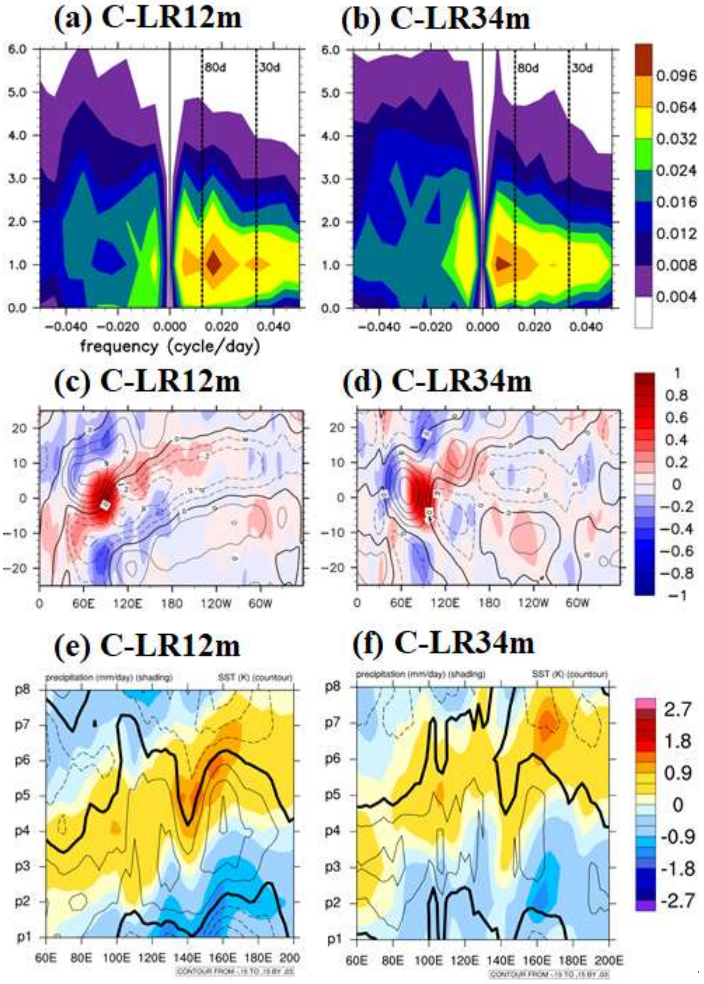
(a) C-LR12m
(b) C-LR34m
80d
30d
frequency (cycle/day)
0.096
0.064
0.032
0.024
0.016
0.012
0.008
0.004
(c) C-LR12m
(d) C-LR34m
(e) C-LR12m
(f) C-LR34m
precipitation (mm/day) (shading)
SST (K) (countour)
2.7
1.8
0.9
0
-0.9
-1.8
-2.7

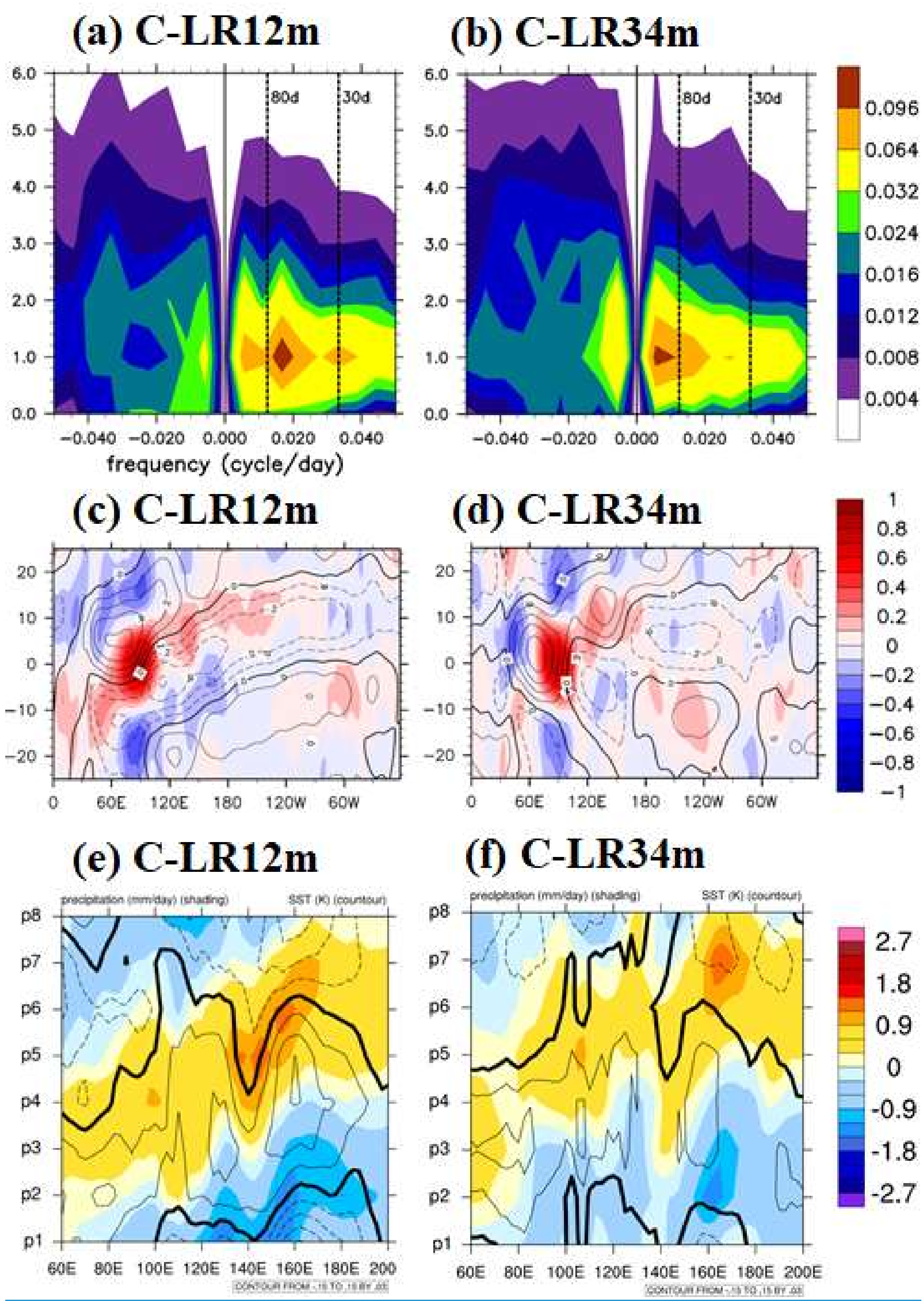

Figure 5. (a)–(b) Same as in Fig. 2(a) but for the C-LR12m and C-LR34m. (c)–(d) Same as in Fig. 2(d) but for the C-LR12m and C-LR34m. (e)–(f) Same as in Fig. 4(a) but for the C-LR12m and C-LR34m.

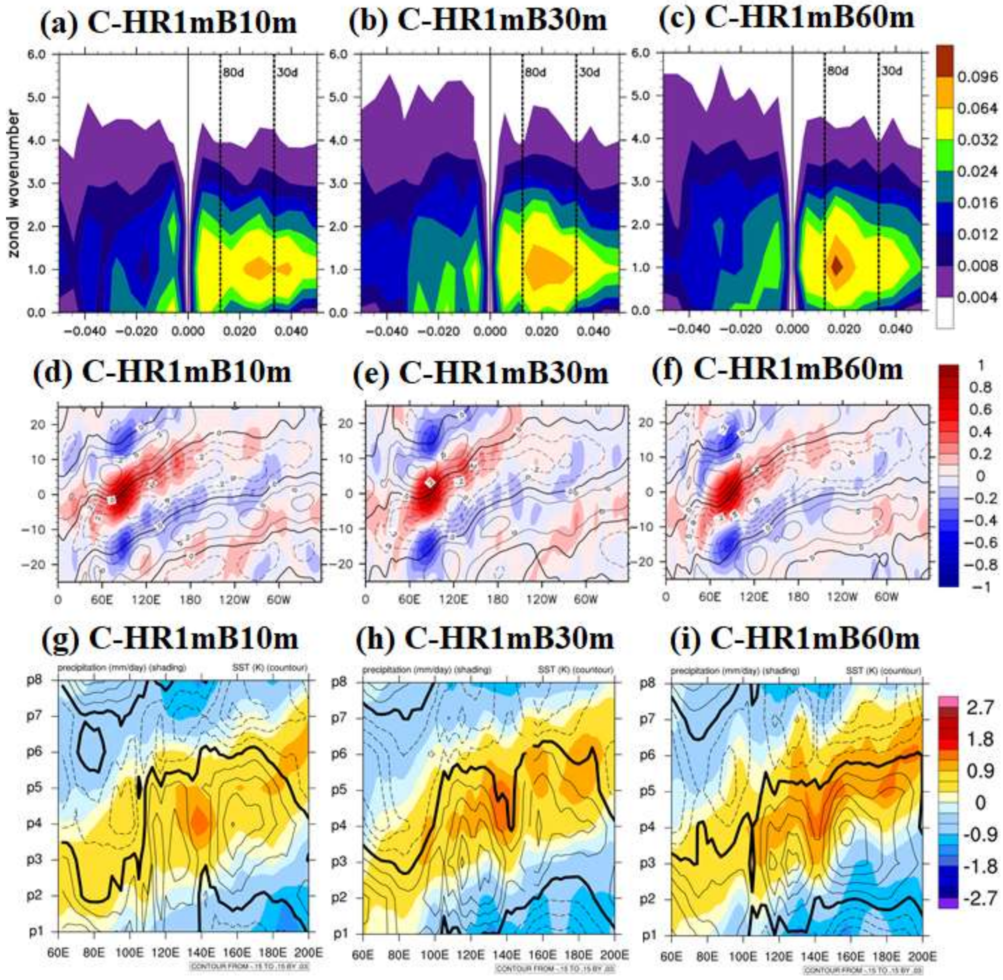
(a) C-HR1mB10m
(b) C-HR1mB30m
(c) C-HR1mB60m
zonal wavenumber
80d
30d
0.096
0.064
0.032
0.024
0.016
0.012
0.008
0.004
(d) C-HR1mB10m
(e) C-HR1mB30m
(f) C-HR1mB60m
(g) C-HR1mB10m
(h) C-HR1mB30m
(i) C-HR1mB60m
precipitation (mm/day) (shading)
SST (K) (countour)
2.7
1.8
0.9
0
-0.9
-1.8
-2.7

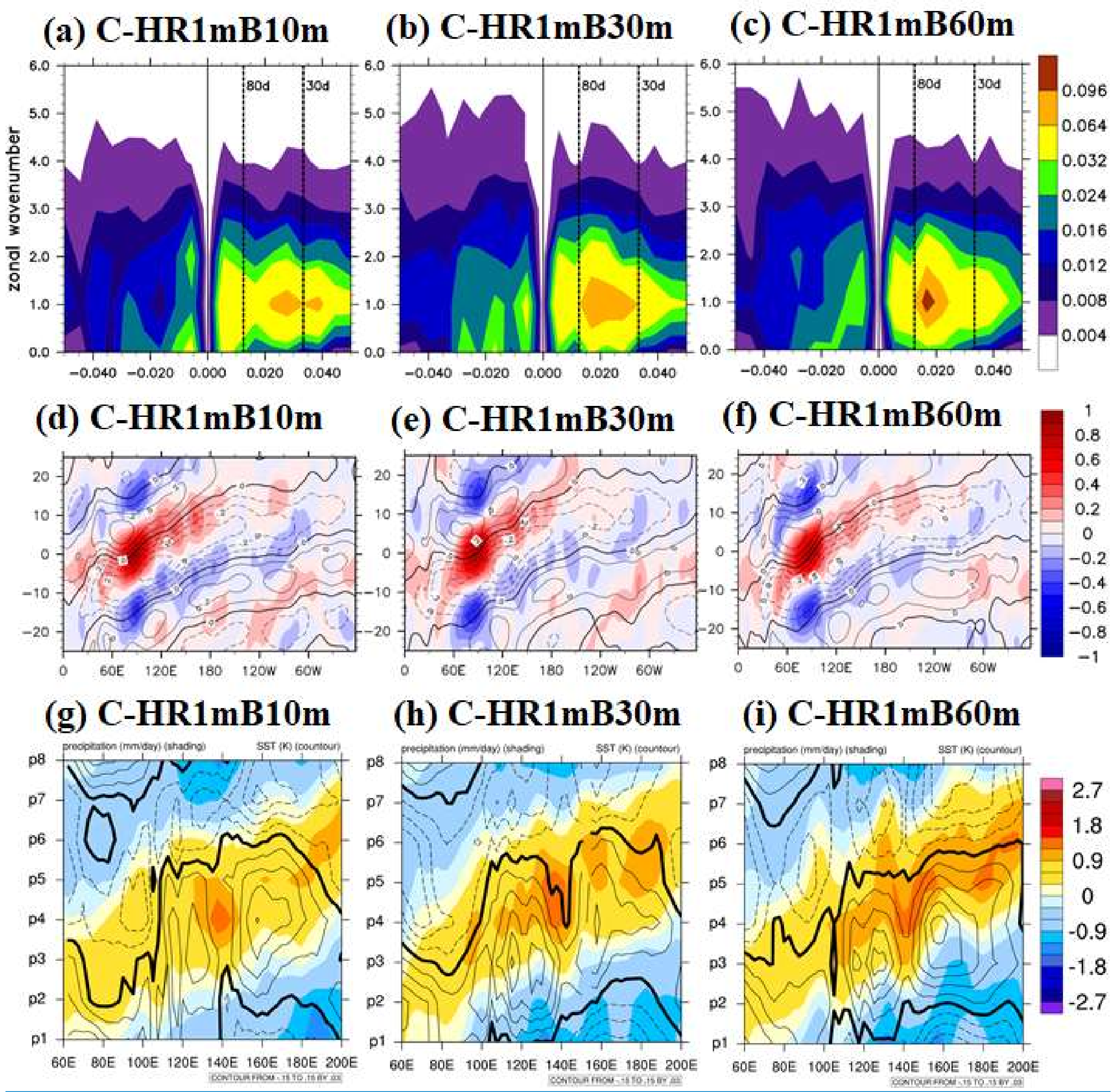

Figure 6. Same as in Fig. 5 but for the C–HR1mB10m, C–HR1mB30m, and C–HR1mB60m.

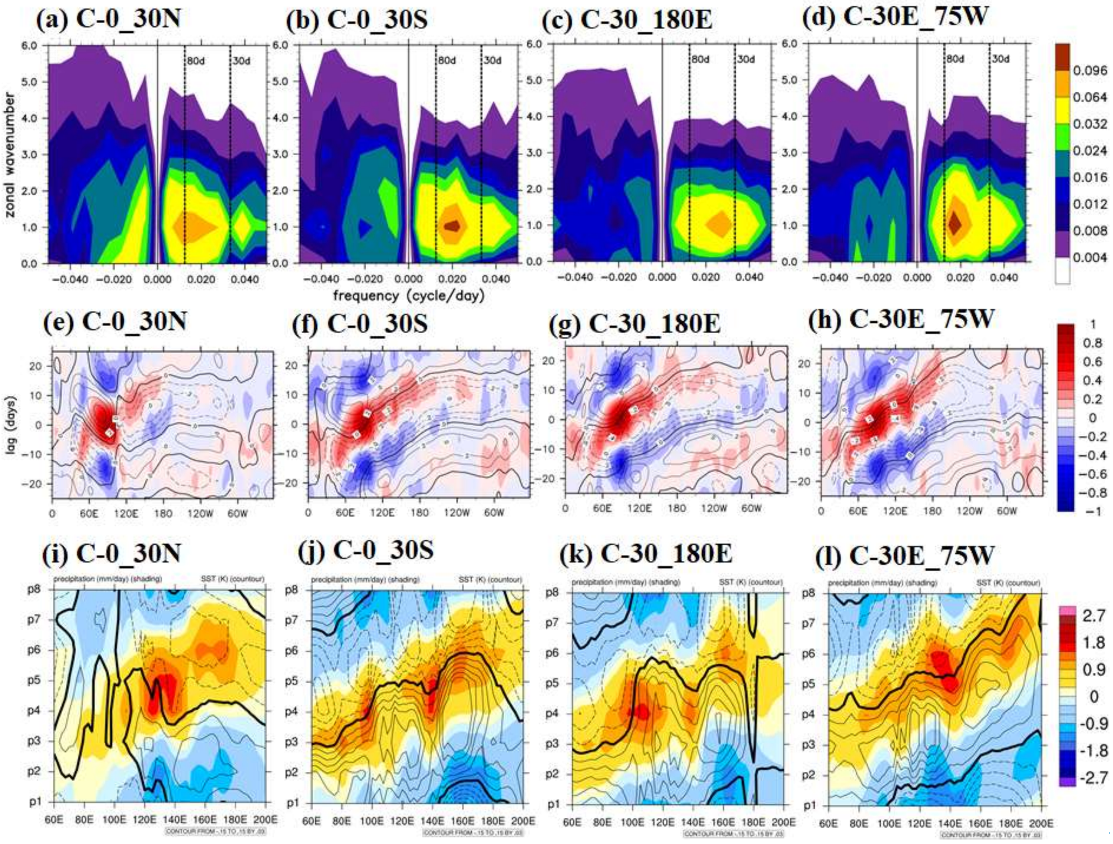
(a) C-0_30N
(b) C-0_30S
(c) C-30_180E
(d) C-30E_75W
zonal wavenumber
frequency (cycle/day)
80d
30d
(e) C-0_30N
(f) C-0_30S
(g) C-30_180E
(h) C-30E_75W
lag (days)
(i) C-0_30N
(j) C-0_30S
(k) C-30_180E
(l) C-30E_75W
precipitation (mm/day) (shading)
SST (K) (countour)
CONTOUR FROM -.15 TO .15 BY .03

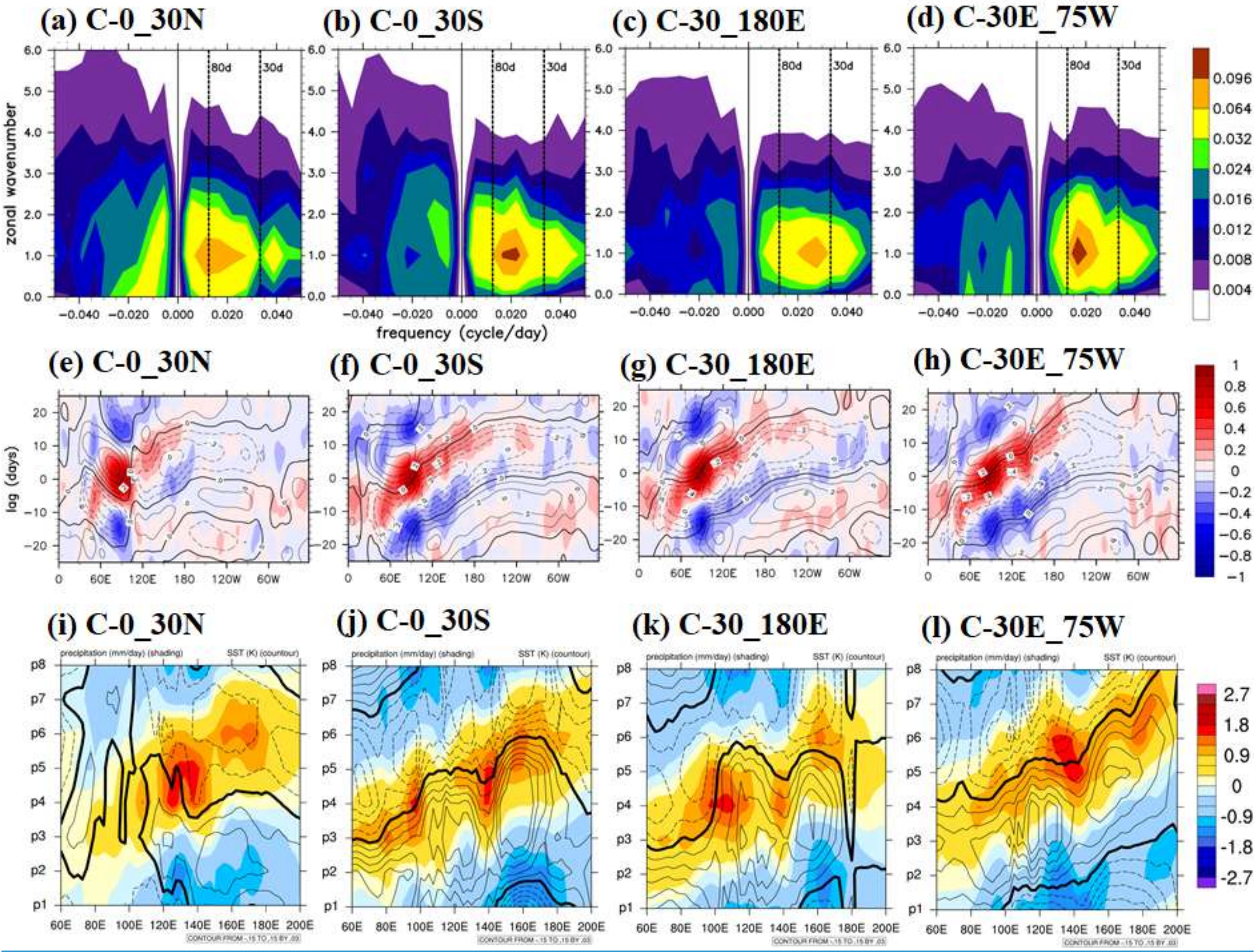

Figure 7. Same as in Fig. 5 but for the C–0_30N, C–0_30S, C–30_180E, and C–30E_75W.

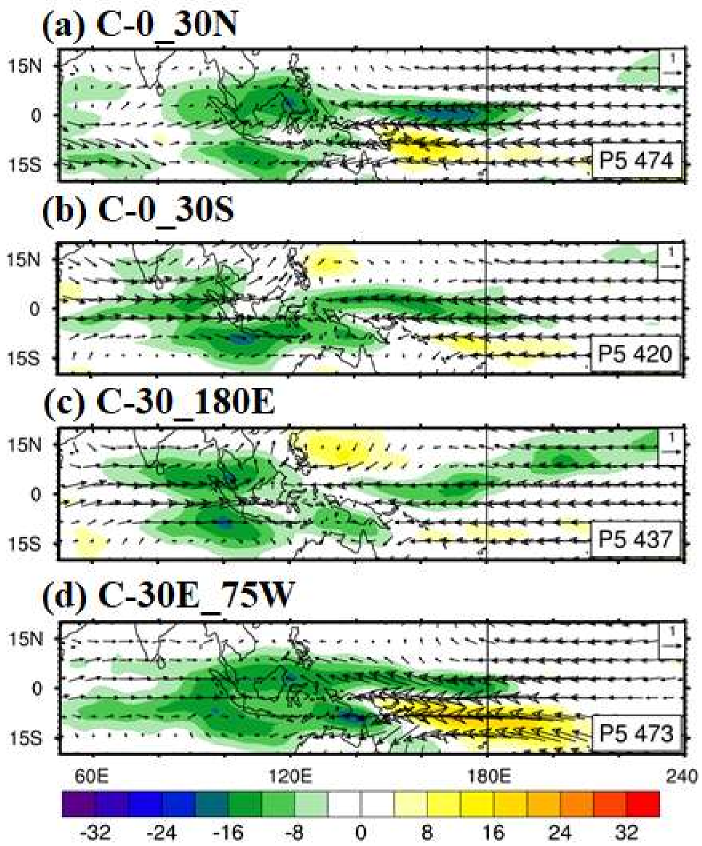
(a) C-0_30N
15N
0
15S
P5 474
(b) C-0_30S
15N
0
15S
P5 420
(c) C-30_180E
15N
0
15S
P5 437
(d) C-30E_75W
15N
0
15S
P5 473
60E
120E
180E
240
-32
-24
-16
-8
0
8
16
24
32

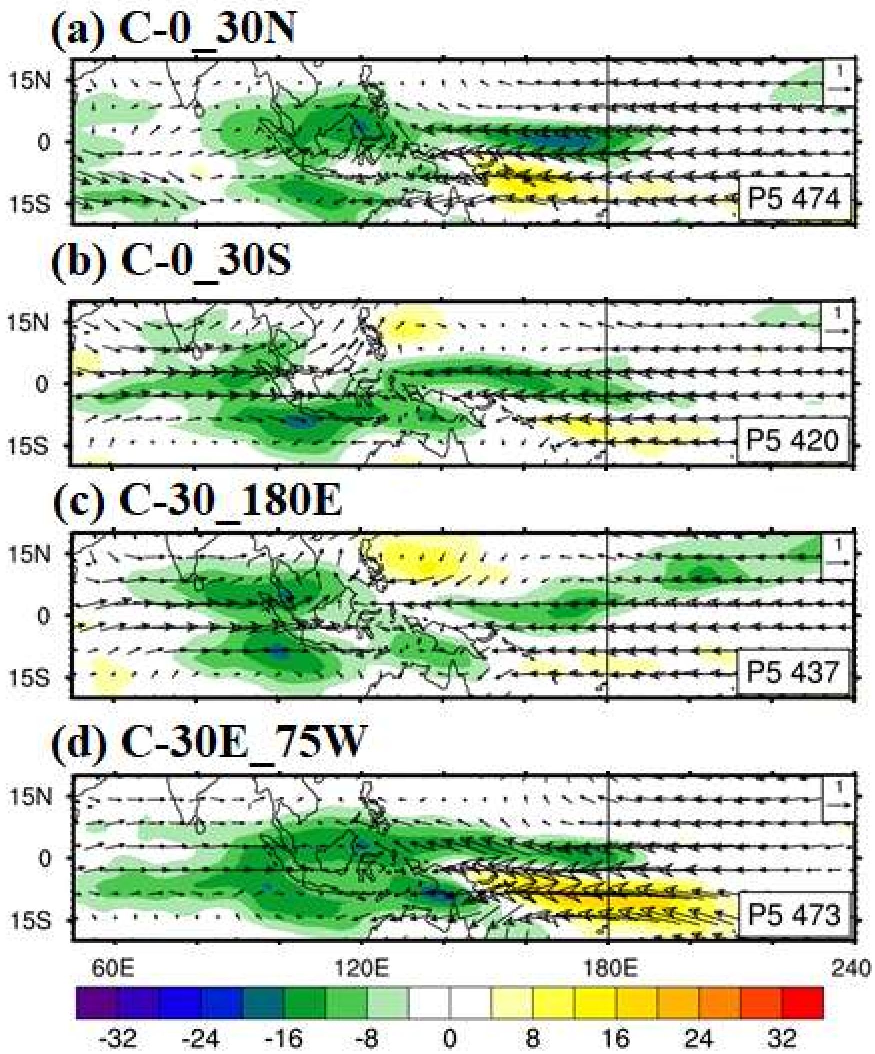

Figure 8. Same as in Fig. 3 but for phase 5 in the C–0_30N, C–0_30S, C–30_180E, and C–30E_75W.

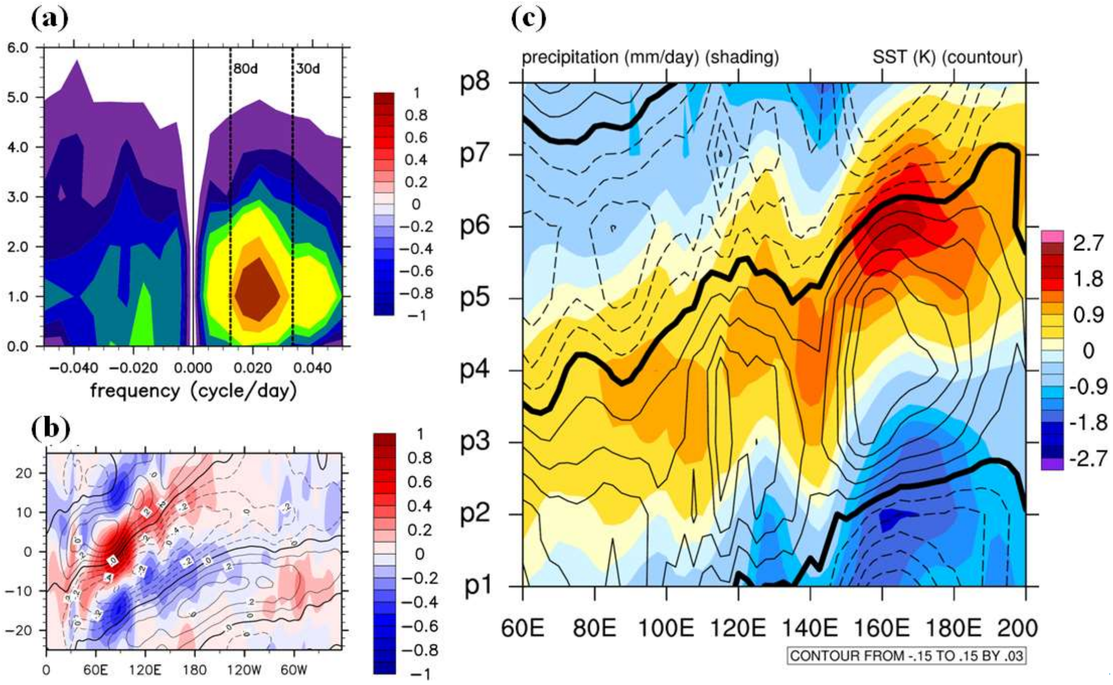

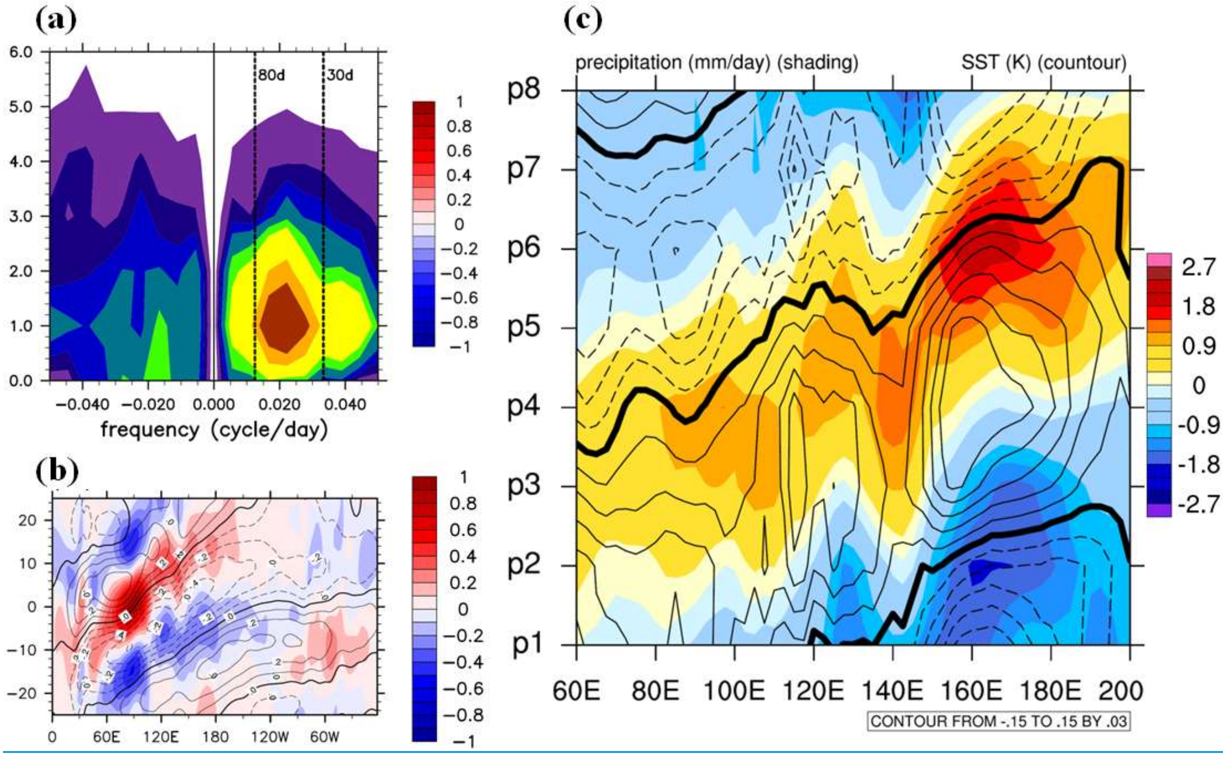

Figure 9. Similar as in Fig. 5 but for the C–30NS–nD.

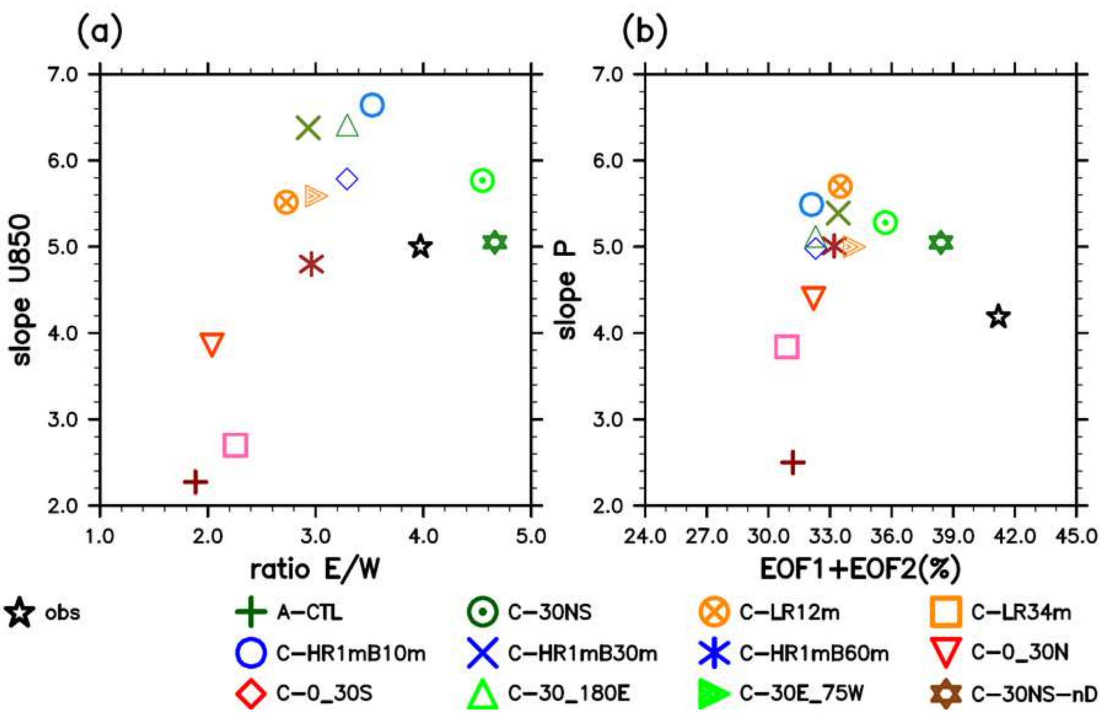

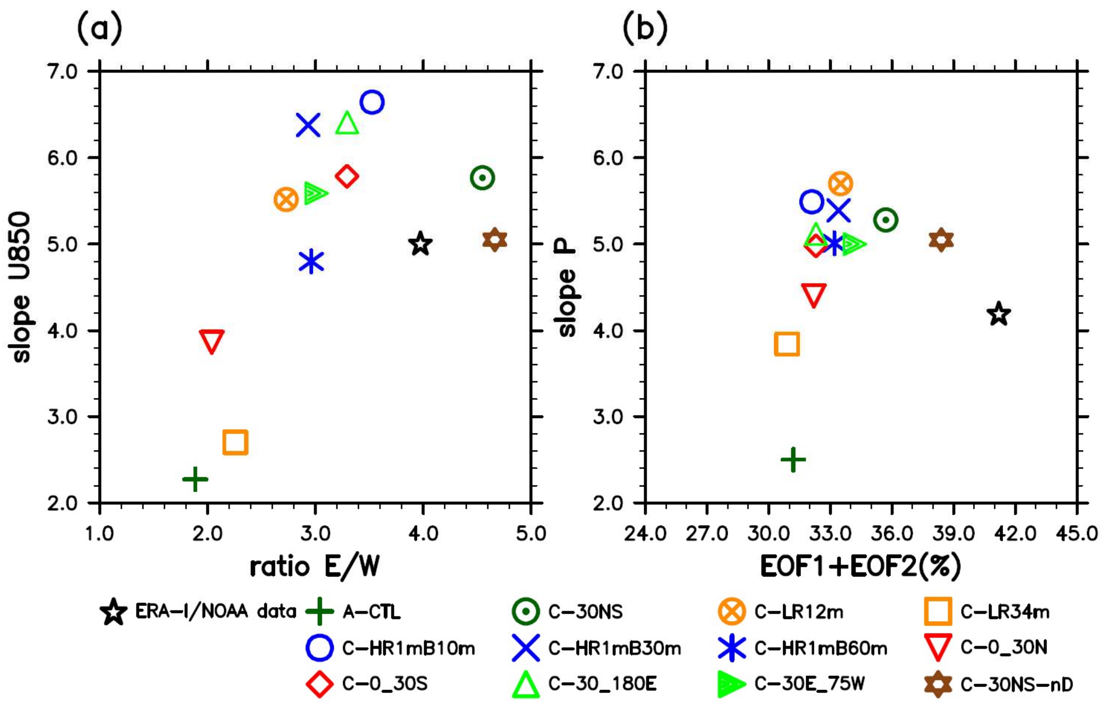

Figure 10. Scattered plots of various MJO indices in ~~observation~~the ERA-I/NOAA data and 12 experiments: (a) power ratio of east/west propagating waves of wavenumber 1–3 of 850-hPa zonal winds (X-axis) with a 30–80-day period and eastward propagation speed of U850 anomaly (Y-axis) from the Hovmöller diagram and (b) RMM1 and RMM2 variance and eastward propagation speed of the filtered precipitation anomaly derived from the Hovmöller diagram.